

Quantum-Controlled Collisions of H₂ Molecules

Nandini Mukherjee*



Cite This: *J. Phys. Chem. A* 2023, 127, 418–438



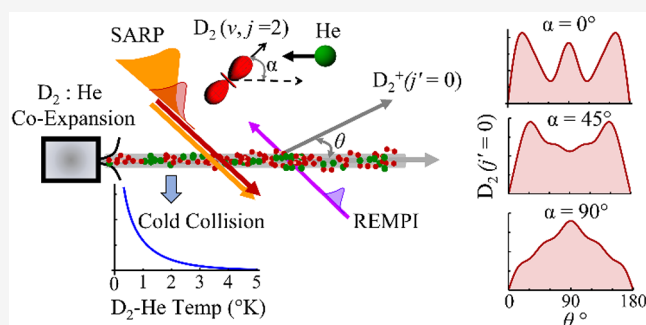
Read Online

ACCESS |

Metrics & More

Article Recommendations

ABSTRACT: The amount of information that can be obtained from a scattering experiment depends upon the precision with which the quantum states are defined in the incoming channel. By precisely defining the incoming states and measuring the outgoing states in a scattering experiment, we set up the boundary condition for experimentally solving the Schrödinger equation. In this Perspective we discuss cold inelastic scattering experiments using the most theoretically tractable H₂ and its isotopologues as the target. We prepare the target in a precisely defined rovibrational (ν , j , m) quantum state using a special coherent optical technique called the Stark-induced adiabatic Raman passage (SARP). ν and j represent the quantum numbers of the vibrational and rotational energy levels, and m refers to the projection of the rotational angular momentum vector j on a suitable quantization axis in the laboratory frame. Selection of the m quantum numbers defines the alignment of the molecular frame, which is necessary to probe the anisotropic interactions. For us to achieve the collision temperature in the range of a few degrees Kelvin, we co-expand the colliding partners in a mixed supersonic beam that is collimated to define a direction for the collision velocity. When the bond axis is aligned with respect to a well-defined collision velocity, SARP achieves stereodynamic control at the quantum scale. Through various examples of rotationally inelastic cold scattering experiments, we show how SARP coherently controls the dynamics of anisotropic interactions by preparing quantum superpositions of the orientational m states within a single rovibrational (ν , j) energy state. A partial wave analysis, which has been developed for the cold scattering experiments, shows dominance of a resonant orbital that leaves its mark in the scattering angular distribution. These highly controlled cold collision experiments at the single partial wave limit allow the most direct comparison with the results of theoretical computations, necessary for accurate modeling of the molecular interaction potential.



INTRODUCTION

The molecular force fields that drive chemistry at the most fundamental level arise from the anisotropic electronic and nuclear charge distributions, whose dynamics is governed by the laws of quantum mechanics. The purpose of a scattering experiment is to probe the anisotropic force field that extends over long distances at the molecular scale. State-resolved scattering experiments studying single-collision events between individual molecules in the gas phase provide the most direct access to the molecular interaction potentials.^{1–7} The probability of scattering measures the degree to which an incoming quantum state is modified by close interaction with its collision partner. To develop an intuitive understanding, let us consider a molecule prepared in an eigenstate $|m\rangle$ of its Hamiltonian H_0 before it encounters the collision partner. In the presence of the partner molecule its state is modified by the interaction Hamiltonian H' . When the first-order perturbation is used, the collision-induced transition probability from the initial eigenstate $|m\rangle$ to a final state $|k\rangle$ is determined by $| \langle k | H' | m \rangle |^2$. Therefore, by measuring the outgoing states for each incoming eigenstate of a complete set, a scattering experiment can, in

principle, determine the interaction Hamiltonian H' . In general, however, in the presence of a large number of incoming states normally available to even small molecular systems, one-to-one correspondence between the incoming and outgoing states is not possible and averaging over states washes out the details of the molecular interactions. Until we eliminate averaging over the states, direct comparison between experimental measurements and theoretical calculations will remain a dream, and as such a theoretical model can be tested only approximately. Such a dream can be realized by designing an ideal scattering experiment that precisely controls the incoming state and measures the final states, as such setting up the boundary conditions for experimentally solving the Schrödinger equation

Received: September 24, 2022

Revised: December 3, 2022

Published: January 5, 2023



$(i\hbar)(\partial\psi/\partial t) = H\psi$, where H represents the Hamiltonian and ψ represents the quantum state of the colliding system.

In this Perspective we will discuss what can be achieved in a near ideal scattering experiment that controls the incoming state defining both the internal and external degrees of freedom. In addition to precisely controlling the energy, the control of molecular alignment, that is, the stereodynamic control in the incoming channel, is essential for mapping the anisotropic molecular forces. Because the quantum state preparation plays a key role in achieving controlled collision, a good portion of this Perspective will be devoted to this topic. However, we want to remind readers that quantum state preparation^{8–15} is already a well-developed field, and we do not intend to review this here. Instead, we will be focusing our discussion on a special case, that is, the quantum control of H_2 and its isotopologue molecules, and illustrating their applications in cold scattering experiments recently conducted in our laboratory at Stanford University.^{16–21} The quantum-state-controlled benchmark experiments are extremely valuable for testing and validating a theoretical model before applying it to a more complex system. We chose H_2 molecules because they are the most theoretically tractable, and as such one can expect one-to-one correspondence between the experimental measurements and theoretical calculations. It is needless to stress the importance of understanding interactions of the most abundant H_2 molecules that have many applications in a variety of physical and chemical processes including combustion and energy storage. Additionally, the collision dynamics of highly vibrationally excited H_2 molecules are of immense interest for understanding and modeling the physics and chemistry of an interstellar medium.^{22–24}

For the gas-phase collisions, the internal degree of freedom of a molecular system is defined by a set of quantum numbers, (n, v, j, m) , that give the electronic state (n), vibrational state (v), and rotational state defined by the internal angular momentum (j), and its projection (m) on a suitable quantization axis. The projection quantum number m defines the molecular frame with respect to a fixed axis in the laboratory frame, thus providing the stereodynamic control necessary to probe the anisotropic van der Waal's interactions.²⁵ Many techniques¹³ ranging from the use of electric^{26–29} or magnetic fields³⁰ for state selection to techniques that use optical pumping to state-prepare molecules^{11,14,31–36} have been developed to realize molecular scattering with the precision of a single quantum state. However, preparation of a large, scattering-sensitive population of H_2 molecules in a single rovibrational (v, j, m) state has been a challenge for a very long time. This is because the homonuclear symmetry forbids infrared excitation, and the Raman pumping is generally weak, requiring large optical intensities that further complicate the optical preparation of a vibrationally excited target state. For one to meet this challenge, a new coherent optical technique called Stark-induced adiabatic Raman passage or SARP^{37–46} was developed; it allows preparation of a large quantity of H_2 and other molecules in a single rovibrational (v, j, m) eigenstate. SARP offers the field-free stereodynamic control by controlling the alignment of the rotational plane or the molecular bond axis with respect to an axis in the laboratory frame. For many homonuclear and symmetric molecules, it is challenging to achieve field-free alignment control, except by using intense ultrashort optical pulses that align them transiently, making them difficult to use in a bimolecular scattering experiment.^{47–49} Additionally, SARP prepares the phase-coherent superposition of degenerate orientational (m)

states within a single rovibrational (v, j) energy state. Because the prepared superposition is stationary in time, it allows the study of quantum interference by coherently controlling the bimolecular collisions.

To reach the full-scale quantum control, one must also control the external degrees of freedom, which describe the relative motion of the colliding particles about their center of mass. In the absence of external force because the linear momentum is a constant of motion, the translational state is described by a plane wave $\sim e^{ikz}$ propagating along the direction of the collision velocity, which can be chosen as the quantization Z axis. The plane wave is composed of an infinitely large number of discrete orbitals l , which are also known as partial waves that describe the rotational motion of the colliding system about the center of mass. Mathematically, the plane wave can be expressed as $e^{ikz} \sim \frac{1}{\sqrt{kr}} \sum_{l=0}^{\infty} i^l \sqrt{(2l+1)} J_{l+1/2}(kr) Y_{l0}(\theta, \varphi)$, where $J_{l+1/2}(kr)$ is the spherical Bessel function, giving the radial amplitude, and $Y_{l0}(\theta, \varphi)$ is the spherical harmonics, giving the angular dependence of the orbital l . The orbital angular momentum l generates the repulsive centrifugal barrier $l(l+1)\hbar^2/2\mu r^2$ that classically prevents the colliding particles from crashing on to each other. When the repulsive centrifugal energy from each of the orbitals is added to the attractive van der Waals potential, the resulting interaction becomes complicated in the presence of a large number of coupled orbitals. Moreover, each orbital angular momentum l couples vectorially with the internal angular momentum j to make a total angular momentum J that must be conserved in a collision process. Theoretical computations to solve the Schrödinger equations for each total angular momentum J can become challenging when there are a large number of orbitals involved in the collision. To gain the clearest possible understanding of the molecular force field, one must restrict the number of incoming orbital states that can be achieved by reducing the collision temperature in the range of a few degrees Kelvin or less. Additionally, for a few low-lying orbitals l , the centrifugal barrier $l(l+1)\hbar^2/2\mu r^2$ can confine a quasi-bound state above the dissociation energy, as depicted by the gray dashed line for an atom–diatom collision in Figure 1. The quasi-bound states, which are referred to as the scattering

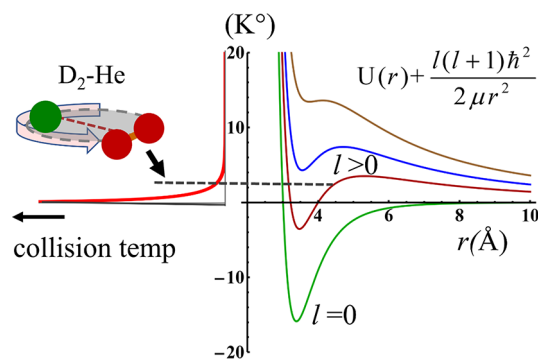


Figure 1. A potential well is created when the centrifugal energy $l(l+1)\hbar^2/2\mu r^2$ of a low-lying orbital is added to the attractive van der Waal's interaction $U(r)$. The potential well can support a quasi-bound state above the dissociation energy. $U(r)$ is drawn using the realistic D_2 -He potential.¹¹⁷ The position of the quasi-bound state represented by the gray dashed line is arbitrary and is used here for the purpose of discussion. The temperature distribution of the cold collision is shown by the red curve on the left. r is the radial distance between the center of mass of D_2 and He, and μ is their reduced mass.

resonances, can be accessed by tunneling through the centrifugal barrier. The tunneling probability is resonantly enhanced when the collision energy matches the energy of the quasi-bound state held behind the barrier. Because the wave function of the quasi-bound state is fairly localized within the well, the collision complex acquires a finite lifetime that could increase the collision cross section by 1 or even 2 orders of magnitude. Indeed, the scattering resonances have made it possible to experimentally observe the low energy scatterings by weak van der Waal's potentials that would otherwise be impossible to measure. To develop an intuitive feeling, let us consider the rotational relaxation of H_2 molecules induced via weak anisotropic interactions. Within the approximation of the first-order perturbation, the probability of state mixing is determined by $|U_{ij}/E_{ij}|^2$, where $U_{ij} (= \langle i|U|j \rangle)$ and E_{ij} represent the anisotropic van der Waals interaction Hamiltonian and the difference energy between the initial $|i\rangle$ and the final $|j\rangle$ rotational states. For the H_2 molecule, U_{ij} is several orders of magnitude smaller than E_{ij} , and as such, the transition probability is generally very small and is often unmeasurable, unless there is a resonance.

Just like those in an optical cavity, the scattering resonances can be formed in various ways from the interference of the incident and scattered matter waves from the interaction potential.⁵⁰ Even with an energy exceeding the barrier height, orbiting resonances can be formed by the interference of incident and reflected partial waves from the inner repulsive wall of the van der Waal's potential.⁵¹ The wave functions associated with the shape resonances that are formed behind the barrier are fairly localized within a short interaction range. These resonances are accessed via tunneling.^{52,53} Then there are Feshbach resonances, which occur when there is coupling between internal and external degrees of freedom associated with the bound state and the scattering state, respectively.^{51,54–57} These resonances are accessed only transiently within the short range of the potential accompanying internal excitation. In each of these resonances, the colliding partners are captured in a short-lived collision complex that strongly enhances the probability of scattering. In this Perspective our discussion focuses specifically on the shape resonances that are encountered in the cold rotational relaxation of neutral H_2 molecules.^{17,58,59} In the presence of a resonance the scattering is dominated by a single orbital providing the centrifugal barrier for the quasi-bound complex. With a single orbital l dominating the scattering process, together with a precisely defined internal angular momentum j , we are able to restrict the possible values of the total angular momentum J . This greatly simplifies both experimental and computational analysis, allowing us to extract in-depth information about the dynamics of quantum interactions.

In recent times, there have been tremendous experimental efforts and excitement in realizing cold collisions in the limit of a single incoming orbital. The s-wave ($l = 0$) and p-wave ($l = 1$) collisions have been realized between a pair of ultracold KRb molecules which were produced by associating ultracold Rb and K atoms.^{60,61} The ultracold collision experiments have demonstrated quantum effects that depend sensitively upon the relative alignment or the collision geometry at the quantum scale.⁶² Alternatively, cold and near-ultracold collisions have been realized in the moving frame of the molecular beams.^{63–65} Although the individual molecular species move at the speed of a few kilometers per second in a molecular beam, their relative velocity can be small, giving a collision energy of a few degrees Kelvin. The molecular beam provides a versatile platform to

study cold collisions between a wide variety of colliding species. Narrow angle crossed beam experiments involving lightweight molecules such as H_2 , CO, and O_2 have made it possible to carry out cold collisions at a few degrees Kelvin, allowing a limited number of partial waves.^{53,57,66–69} In these experiments the collision energy was tuned by varying the crossing angle, detecting Feshbach and shape resonances in much the same way as molecular lines are detected using optical spectroscopy. External-field-induced deceleration of molecular beams combined with the velocity map imaging (VMI) of the angular distribution have further advanced the scope of studying the resonant scattering in a crossed beam experiment. Imaging the angular distribution at highly resolved collision energies in the sub-Kelvin temperature range, Meerakker's group studied the benchmark NO-He collision in the presence of Feshbach resonances.⁶⁸ Their study captured collision dynamics at the resolution of a few resonant partial waves. The merging of two molecular beams using external electric or magnetic fields has brought major advances, realizing cold collisions in the range of a few milliKelvins along with high-resolution tuning of the collision energy.^{70–74} Studying the penning ionization reactions of H_2 with an electronically excited He atom in a merged molecular beam, Narevicius and his co-workers demonstrated shape resonances that arise exclusively from the anisotropic interactions of rotating H_2 molecules.^{71,75} These and many recent high-resolution cold scattering experiments at the level of a single orbital together with the detailed theoretical computations have greatly advanced our understanding of quantum interactions.^{16–21,53,66,76–80}

Because of their light weights, H_2 and its isotopologues allow only a few low-lying incoming orbitals, $l = 0, 1, 2, 3$, to participate in a cold collision with the temperature near 1 K, thus making it easier to experimentally probe the scattering resonances without requiring a complex cooling procedure. Additionally, because the internal energy levels of H_2 are sparse, the energy redistribution in a cold collision is substantially simplified, making it possible to identify the individual partial wave resonances. Extensive theoretical studies have been done on inelastic collisions of vibrationally excited H_2 with He,^{81,82} H,^{78,83} D,⁸⁴ Ar,^{85,86} and H_2 ^{77,87} that predicted shape resonances at a temperature of a few degrees Kelvin. These studies stressed the importance of vibrational excitation in long-range van der Waals interactions. Unfortunately, until recently, preparation of a large population of hydrogen molecules in a single highly excited vibrational state has proven to be experimentally challenging, and so, many of these theoretical predictions have yet to be verified. Although many inelastic scattering experiments have been performed using molecular hydrogen or its isotopologues,^{88–92} until the development of SARP, none have been conducted at low temperature with highly vibrationally excited and aligned H_2 molecules. SARP preparation of vibrationally excited target states has allowed us to observe the cold collisional relaxation of pure *o*- or *p*- H_2 . Combining the molecular beam method with SARP's ability to prepare a spatially aligned single rovibrational quantum state has opened completely new possibilities for cold scattering experiments that could challenge the most sophisticated theoretical calculations.

Before illustrating the scattering experiments of SARP-prepared H_2 , we present a brief description of how cold collisions are achieved in our laboratory within a single molecular beam (in the section "Cold Collision in the Moving Frame of a Mixed Supersonic Beam"). Because SARP plays the key role in controlling the internal quantum state and the

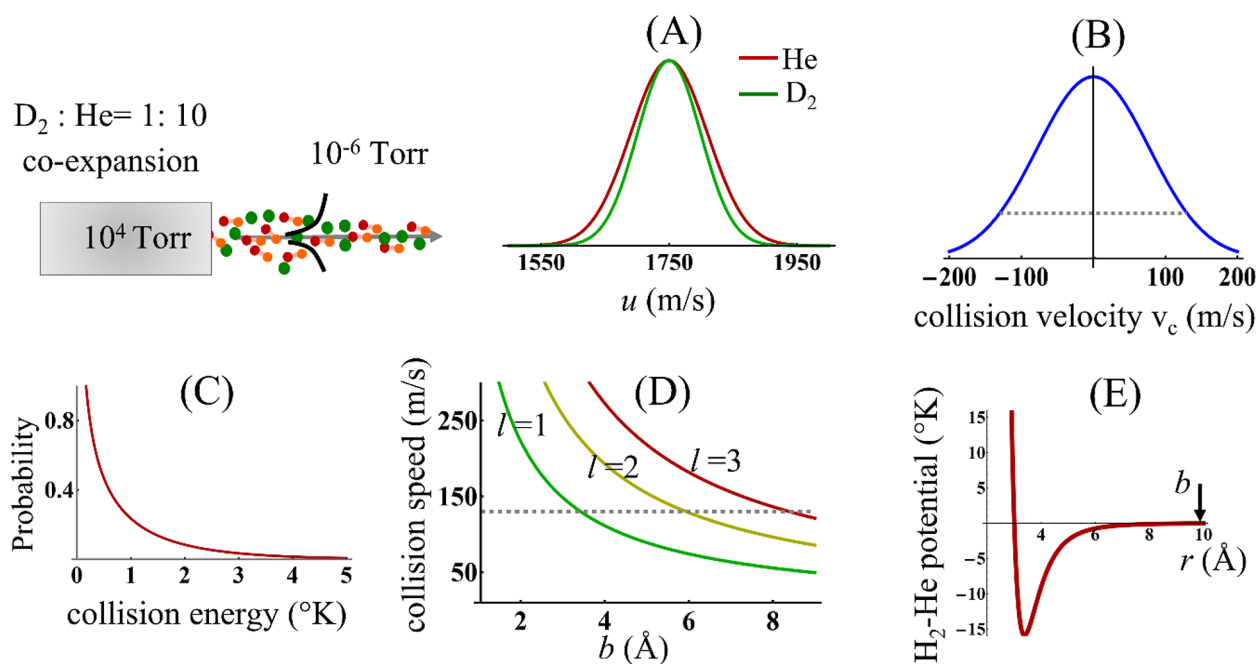


Figure 2. Cold collision achieved by co-expanding partner molecules in a single supersonic beam. (A) Distributions of the laboratory frame velocities u (m/s) for D₂ (green) and He (red): $f_{D_2}(u) = e^{-((u-1750)/70)^2}$, $f_{He}(u) = e^{-((u-1750)/85)^2}$. (B) D₂-He collision velocity distribution. The dotted line shows the range of velocities with which 90% of the collisions take place. (C) D₂-He collision temperature distribution. (D) Partial wave contours defined by $b = \sqrt{l(l+1)} \hbar / \mu v_c$ as a function of the collision speed v_c (m/s) and impact parameter b for $l = 1, 2, 3$. (E) H₂-He van der Waal's potential. (D) and (E) show that for a given orbital l as the collision speed decreases, the impact parameter b increases and finally falls outside the interaction range, thus effectively switching off the interaction.

collision geometry, we present an elaborate description of SARP in the section “SARP Control of Internal States and Collision Geometry”. In the section “Method of Partial Wave Analysis for the Rotationally Inelastic Cold Scattering Experiments”, we describe the partial wave analysis that is used to interpret the results of the cold scattering experiments. The section “Experimental Study of Cold $j = 2 \rightarrow j' = 1$ and $j = 2 \rightarrow j' = 0$ Rotational Relaxations” illustrates the benchmark cold scattering experiments using SARP-prepared H₂ molecules. We conclude in the section “SARP Opens New Avenues to Experimentally Probe the Quantum Mechanism of Molecular Interactions” with a discussion of future possibilities of quantum-controlled collisions.

■ COLD COLLISION IN THE MOVING FRAME OF A MIXED SUPERSONIC BEAM

In our laboratory at Stanford University scattering experiments have been conducted using molecular beams in a differentially pumped vacuum chamber. The molecular beam is formed by supersonically expanding a mixed molecular gas containing the colliding partners using an Even-Lavie pulsed valve. As the gas mixture expands adiabatically from a high-pressure (~ 10 – 20 atm) region into the vacuum, the velocity slip between the partner molecules in the beam reduces, bringing the collision temperature down to a few degrees Kelvin as shown in Figure 2 for the case of D₂-He co-expansion.⁹³ A highly collimated molecular beam with divergence < 12 mrad is formed using a skimmer (diameter ~ 1 mm) placed at a distance of approximately 8–10 cm from the pulsed valve. The supersonic beam with a sharply defined velocity provides a direction in space with respect to SARP aligning the molecular bond axis, defining a specific geometry for collision. We like to emphasize

that cold collisions within a highly collimated beam can be treated as 1D, which greatly simplifies the analysis of a scattering experiment. Reaction products are detected state-selectively, using resonance-enhanced multiphoton ionization (REMPI) in a mass spectrometer that is connected to our molecular beam vacuum chamber. The laser beams for SARP and REMPI intersect the molecular beam transversely from opposite directions. The experimental arrangement to observe scattering in a single beam is shown schematically in Figure 3.

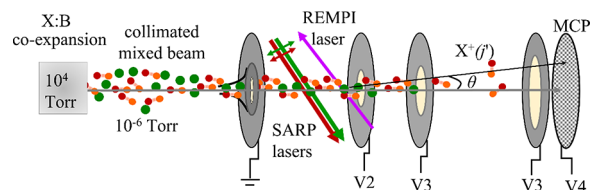


Figure 3. Schematic of a cold scattering experiment within a co-expanded mixed supersonic beam containing the colliding partners (X and B). Polarized SARP laser beams (red and green) prepare the target molecule X (H₂, HD, or D₂) in a given rovibrational m eigenstate (v, j, m), where m refers to the projection of the rotational angular momentum j along the molecular beam direction. The colliding partner B (He, Ne, H₂, D₂, or HD) is left unprepared. The collision product is ionized state-selectively using REMPI with tunable vacuum ultraviolet pulses and detected on a multichannel plate (MCP) following a passage through the time-of-flight mass spectrometer, which is attached to the high-vacuum scattering chamber. V2–V4 represent the voltages applied to the various electrodes of the mass spectrometer fulfilling the space-focusing condition. The scattering angle θ is extracted from the time-of-flight measurement of the product. All laser beams intersect the molecular beam transversely.

A collimated mixed molecular beam not only provides a unidirectional collision velocity but also brings the collision temperature down to a few degrees Kelvin, limiting the number of involved partial waves. As an example, let us consider the co-expanded beam of D₂ and He shown in Figure 2. Figure 2A shows the laboratory frame longitudinal velocity distribution $f_{D_2}(u)$ and $f_{He}(u)$ for D₂ and He in the mixed beam. The velocity distributions are determined from the measurements of their time-of-flight (TOF) distributions in the ionization mass spectrometer (see Figure 3). To reach the precision of collision energy of a few degrees Kelvin, the time-of-flight is measured carefully, taking into account the recoil from the photoelectron generated in the ionization process, a detailed description of which can be found elsewhere.^{93,94} The D₂-He collision velocity (the same as the relative velocity) distribution shown in Figure 2B is found by convoluting the longitudinal velocity distributions of the individual collision partners (Figure 2A), which is expressed as $f(v_c) = \int_{-\infty}^{\infty} f_{D_2}(u)f_{He}(u - v_c) du$. In the laboratory frame, even though the individual particles are moving at a speed of a few kilometers per second, the slip between their velocities (magnitude of v_c) can be quite small (Figure 2B), resulting in a small collision energy of a few degrees Kelvin (as shown in Figure 2C). The classical impact parameter b is related to the collision speed v_c using the semiclassical equation, $b = \sqrt{l(l+1)} \hbar / \mu v_c$. Therefore, for a given orbital with angular momentum l , a smaller collision speed v_c would require a larger impact parameter b . With the reduction of collision speed as the impact parameter for a given orbital becomes larger, exceeding the range of van der Waal's interaction (Figure 2D,E), that orbital becomes less important and can be neglected. For the range of D₂-He collision velocity in the mixed beam (Figure 2B), only a few incoming orbitals, $l = 0, 1, 2, 3$, are meaningfully involved in the collision process (Figure 2D,E). In the presence of a resonance, only one of these orbitals will dominate the scattering process.

■ SARP CONTROL OF INTERNAL STATES AND COLLISION GEOMETRY

To obtain a good signal-to-noise ratio in a scattering experiment having cross sections of $\sim 1 \text{ \AA}^2$, we require at least 10^9 target molecules prepared in a single rovibrational quantum state (v, j). The traditional off-resonant Raman pumping that uses two-photon resonance to transfer the population to a desired vibrationally excited state can be extremely weak in the absence of a real intermediate state. For H₂ and many diatomic molecules with a large separation between the ground and excited electronic states, the resonant Raman process requires the use of extreme ultraviolet lasers that may complicate the pumping process by ionizing the intermediate states. SARP is based on off-resonant Raman pumping that combines a pair of intense visible or infrared laser pulses to meet the two-photon Raman resonance, as shown in Figure 4.

To compensate for the weak Raman coupling, SARP uses large optical pulse intensities that induce a dynamic Stark shift of the Raman resonance. In the presence of a time-dependent resonance, at first it seems impossible to achieve consistent population transfer to a rovibrational excited state. SARP takes advantage of this dynamic Stark shift to control the crossings of the optically dressed adiabatic eigenstates and achieves the near-complete population transfer to a desired target state. In the following we explain how SARP carries out the population

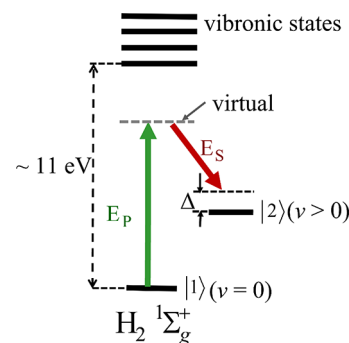


Figure 4. Raman pumping of a rovibrational eigenstate within the ground electronic state H₂¹Σ_g⁺ using visible pump and Stokes laser pulses, both of which are far detuned from the single-photon resonance between the ground and the first excited electronic state. The two-photon resonance $\omega_{21} = \omega_p - \omega_s$ is closely satisfied by the pump (ω_p) and Stokes (ω_s) laser frequencies. The two-photon detuning Δ ($\sim 10^{-2}$ THz) is much smaller than the Raman frequency ω_{21} (~ 100 THz). The gray dashed line shows the position of the virtual intermediate.

transfer using a pair of partially overlapping nanosecond laser pulses. The time-dependent two-photon resonant excitation can be described by the modified Schrödinger equation involving a 2×2 optical Hamiltonian:⁹⁵

$$i \frac{d}{dt} \begin{pmatrix} C_1 \\ C_2 \end{pmatrix} = \begin{pmatrix} -\Delta/2 & \Omega_R \\ \Omega_R & \Delta/2 \end{pmatrix} \begin{pmatrix} C_1 \\ C_2 \end{pmatrix} \quad (1)$$

C_1 and C_2 represent the quantum mechanical amplitudes for the initial and final rovibrational states. The off-diagonal element Ω_R of the interaction Hamiltonian represents the two-photon Raman Rabi frequency and is responsible for mixing the initial and target states. Ω_R is given by the product of the optical fields E_p and E_s of the pump and Stokes laser pulses:^{38,45}

$$\Omega_R = \frac{E_p E_s}{\hbar} r_{12} \quad (2)$$

In eq 2 r_{12} is the Raman coupling between the initial and final vibrational states which is determined by the overlap of the vibrational wave functions, that is, $r_{12} \propto \mu_{v_1 v'} \mu_{v' v_2}$, where $\mu_{v_1 v'}$ and $\mu_{v' v_2}$ are the transition dipole moments connecting the initial v_1 and the target v_2 states via the electronically excited vibronic state v' . Δ in eq 1 is the Stark-induced dynamic Raman detuning given by^{38,45}

$$\Delta(t) = \Delta_0 - \frac{1}{\hbar} [\alpha_{12}(\omega_p) |E_p|^2 + \alpha_{12}(\omega_s) |E_s|^2] \quad (3)$$

In eq 3 $\alpha_{12}(\omega)$ is the difference polarizability of the initial and final states at the optical frequency ω . The large optical intensities $I_{p,s} \propto |E_{p,s}|^2$ of the pump and Stokes pulses induce time-dependent change in the two-photon detuning Δ during the course of Raman excitation. We will show that, under the nonstationary resonance condition, the population can still be transferred efficiently by manipulating the adiabatic eigenstates of the optical Hamiltonian. The adiabatic eigenstates are obtained by diagonalizing the 2×2 optical Hamiltonian appearing on the right-hand side of eq 1. They are given by^{44,45}

$$|+\rangle = \sin \theta |1\rangle + \cos \theta |2\rangle \quad (4a)$$

$$|-\rangle = \cos \theta |1\rangle - \sin \theta |2\rangle \quad (4b)$$

The energy eigenvalues of the adiabatic states are $E_{\pm} = \pm \frac{\tilde{\Omega}}{2}$, where $\tilde{\Omega} = \sqrt{4\Omega_R^2 + \Delta^2}$.

The projection of the adiabatic states onto the bare states $|1\rangle$ and $|2\rangle$ are defined by $\cos \theta = \sqrt{\frac{\tilde{\Omega} + \Delta}{2\tilde{\Omega}}}$ and $\sin \theta = \sqrt{\frac{\tilde{\Omega} - \Delta}{2\tilde{\Omega}}}$. Because at the initial time ($t = 0$) the entire population is confined within the ground state $|1\rangle$, eq 4a and eq 4b suggest that, in general, the interaction with optical pulses will result in a time-dependent superposition of the two adiabatic eigenstates:

$$\psi(t) = \sin \theta |+\rangle e^{i\tilde{\Omega}t/2} + \cos \theta |-\rangle e^{-i\tilde{\Omega}t/2} \quad (5)$$

The state in eq 5 creates population oscillations both in the initial state $|1\rangle$ and in the final state $|2\rangle$, which are known as the Rabi oscillations (Figure 5). As we do not have control over the

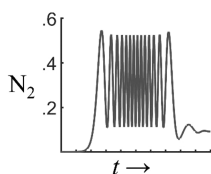


Figure 5. Rabi oscillation of the population in the Raman-pumped rovibrationally excited state $|2\rangle$ as a result of mixing the light-induced adiabatic eigenstates $|+\rangle$ and $|-\rangle$. N_2 represents the fractional population transfer from the initial state $|1\rangle$ to the target state $|2\rangle$.

phase of the Rabi oscillations, to obtain a consistent population transfer, we must avoid mixing of the adiabatic states and instead use one of them to transfer the population from the initial state to the target state. This can be achieved in the following way by manipulating the projections $\cos \theta$ and $\sin \theta$ in eq 4a and eq 4b. As an example, let us consider the special situation depicted in Figure 6A, where the time-dependent detuning Δ is large and

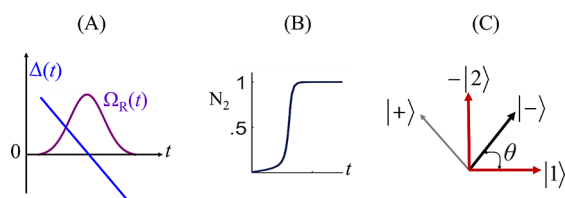


Figure 6. Adiabatic population transfer by changing the detuning Δ during excitation. (A) Sweeping of the detuning Δ (blue) from a large positive value to a large negative value such that the resonance ($\Delta = 0$) is crossed near the peak of the two-photon Rabi frequency Ω_R (purple). (B) Complete population transfer to the rovibrationally excited state $|2\rangle$ is achieved following the pulsed excitation after Δ becomes large and negative. N_2 gives the fractional population transfer from the initial state to the target state. (C) Rotation of the adiabatic eigenstates $|-\rangle$ and $|+\rangle$ in the Hilbert space of the bare states $|1\rangle$ and $|2\rangle$.

positive in the initial part of the excitation, crosses resonance where the Rabi frequency Ω_R reaches its peak, and then becomes large and negative near the end of excitation. Under this condition, at the initial time ($t \approx 0$) when $\Delta \gg \Omega_R$, we have $\cos \theta \approx 1$ and $\sin \theta \approx 0$, so the adiabatic state $|-\rangle$ aligns with the initial bare state $|1\rangle$. As a result, the entire population of the initial ground state is loaded into the adiabatic state $|-\rangle$, whereas the other adiabatic state $|+\rangle$ is left empty. During the course of excitation, the time-dependent detuning Δ and the Raman Rabi frequency Ω_R modulate the projection coefficients $\cos \theta$ and $\sin \theta$, thus mixing the bare states $|1\rangle$ and $|2\rangle$ within the single

adiabatic state $|-\rangle$. Near the end of excitation as Δ becomes large and negative, $\sin \theta \approx 1$ and $\cos \theta \approx 0$, transferring the entire population from the initial state $|1\rangle$ to the target state $|2\rangle$, as shown in Figure 6B. The time evolution of the adiabatic state can be visualized as the rotation in the Hilbert space spanned by the bare states $|1\rangle$ and $|2\rangle$ (Figure 6C). Initially, the adiabatic state $|-\rangle$ aligns with the ground state $|1\rangle$, and then under the optical excitation it slowly rotates, finally aligning with the target state $|2\rangle$. Note that there is no special preference over the adiabatic states; either one can be used to transfer the population. For efficient transfer of the population, the adiabatic states $|-\rangle$ and $|+\rangle$ must remain isolated, requiring that the time evolution must progress at a sufficiently slow rate to maintain the condition of adiabaticity given by^{44,45}

$$\left| \frac{d\theta}{dt} \right| < \Delta E_{\pm} = \tilde{\Omega} \text{ or, equivalently, } \frac{d\Delta}{dt} < 4\Omega_R^2 \quad (6)$$

The condition given in eq 6 is known as the Landau–Zener condition. The required resonance crossing of the detuning Δ that induces the adiabatic evolution of the dressed states (eq 4a) can be experimentally realized by mixing a strong laser pulse (either pump or Stokes) with a weaker and delayed laser pulse, as shown in the upper panel of Figure 7. The laser pulses must be

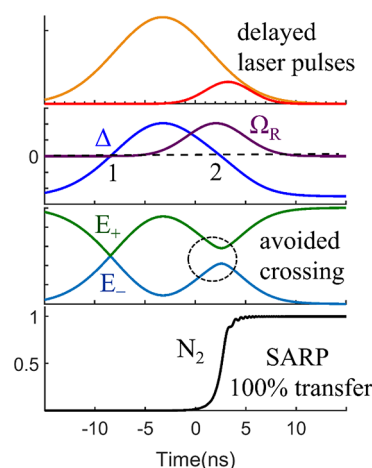


Figure 7. SARP transfers the complete population to the rovibrational target state $|2\rangle$. Top panel: Strong Stokes laser pulse (yellow) partially overlapping in time with a weaker pump pulse (red). Second panel from top: Stark-induced Raman detuning Δ (blue) and the two-photon Rabi frequency Ω_R (purple) as functions of time. The zero crossing of the detuning Δ is explicitly marked by the numbers 1 and 2. Third panel from the top: Energies E_{\pm} of the adiabatic eigenstates during the course of excitation. At the second zero crossing of the detuning, in the presence of a strong Rabi frequency Ω_R , the crossing of the adiabatic states (E_{\pm}) is avoided. Bottom panel: The complete population is transferred from the initial state $|1\rangle$ to the target state $|2\rangle$ at the avoided crossing. N_2 gives the fractional population transfer from the initial to the target state. The SARP temporal dynamics shown here were calculated by numerically solving the Schrödinger equation (1) for H_2 molecules using realistic molecular and laser parameters.

single mode to be able to coherently control the population transfer. We numerically solve eq 1 with this pulse sequence. Figure 7 shows that the complete population can be transferred to the target state. The middle and third panels of Figure 7 show that the detuning Δ crosses zero (resonance) twice, and only the second crossing becomes avoided in the presence of the weaker (pump) pulse, making a sufficiently strong Rabi frequency Ω_R

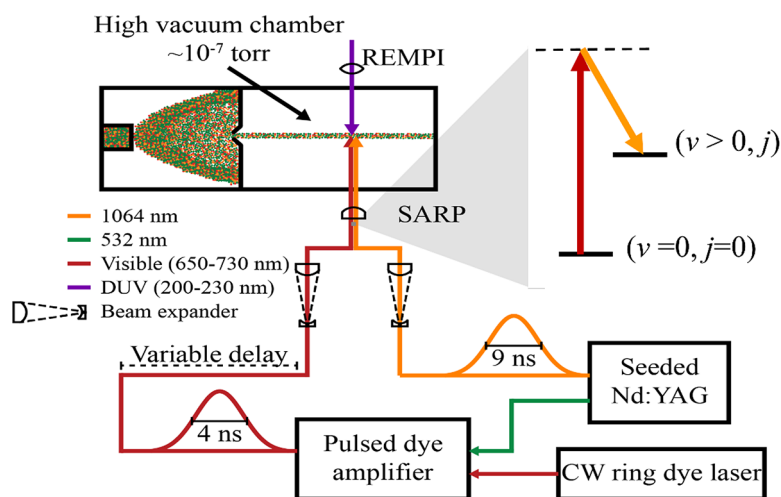


Figure 8. Schematic of SARP experimental setup. A single-mode strong Stokes laser pulse (yellow) is mixed with a weaker single-mode pump laser pulse (red) to satisfy the two-photon Raman resonance. The strong single-mode Stokes (1064 nm, 9 ns, yellow) pulse is derived from an injection-seeded Nd^{3+} :YAG laser, the second harmonic of which pumps a seeded dye pulse amplifier to generate the single-mode pump pulse (655 nm, 4 ns, red) with appropriate fluence required to meet the SARP's adiabaticity condition. The weaker pump pulse is optically delayed before being combined with the strong Stokes pulse. Both laser pulses are brought into focus within the molecular beam. The optimum overlap of the pump and Stokes pulses are achieved by controlling their divergence using telescopes in their respective optical beam paths. The SARP-prepared target states are probed using (2 + 1)-resonant-enhanced multiphoton ionization (REMPI) with tunable deep UV pulses (~ 200 nm) that counterpropagate with respect to the SARP laser beams. All lasers intersect the molecular beam transversely. The REMPI probe beam is placed downstream from the SARP preparation site to avoid ionization and Stark shift during the operation of SARP.

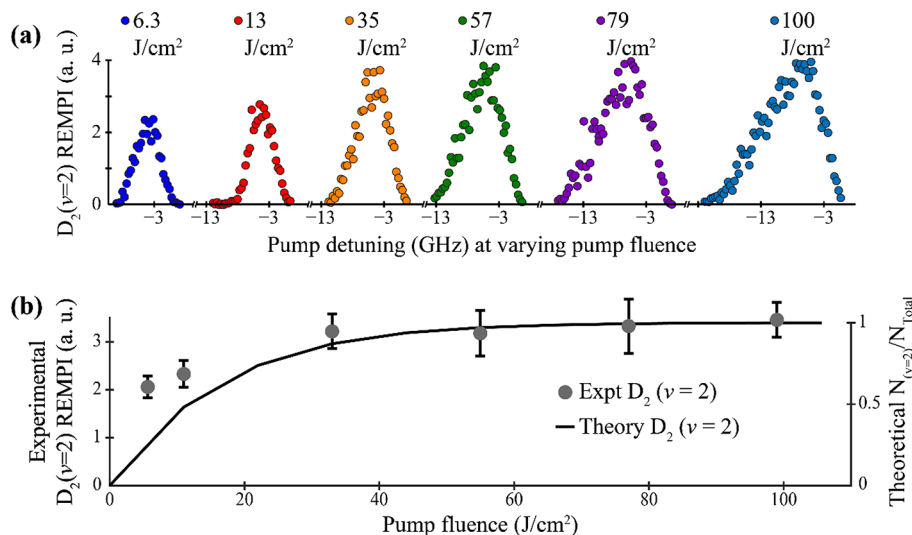


Figure 9. Saturation of $\text{D}_2(v=0, j=0) \rightarrow \text{D}_2(v=2, j=0)$ Raman transition as a function of pump (655 nm) fluence (J/cm^2) at a pump to Stokes delay of 6.5 ns confirms near-complete population transfer to the ($v=2$) target state. (a) Spectral response of the REMPI signal from $\text{D}_2(v=2, j=0)$ as a function of the pump detuning (GHz) for various pump fluences at a fixed Stokes pulse fluence of $2500 \text{ J}/\text{cm}^2$. (b) Comparison of the theoretically calculated peak spectral response to that measured experimentally as a function of the pump fluence shown in (a). Figure reprinted from ref 45. Copyright 2019 AIP Publishing.

that satisfies the Landau–Zener condition of eq 6. The complete population is transferred to the target state during the second crossing, as shown in the bottom panel of Figure 7. A schematic of the SARP experimental setup is shown in Figure 8.

The near-complete population transfer from the initial state to the target state is demonstrated by the threshold behavior of the measured target population against the fluence of the pump lasers, which is a hallmark of adiabatic passage, as illustrated in Figure 9b for the preparation of the $\text{D}_2(v=2, j=0)$ state. Although the threshold behavior against laser fluence looks very much like saturation, we must realize that the population transfer is not saturated but does reach the 100% level. Later, we

will show that this apparent saturation is accompanied by near-complete depletion of the initial state population (Figure 11). With increasing fluence the frequency detuning over which the complete population is transferred widens, as can be seen in Figure 9a. SARP has demonstrated the near-complete population transfer of H_2 and its isotopologues to a variety of vibrationally excited ($v=1, 2, 4, 7$), and rotationally oriented (j, m) quantum states.^{36,39,40,42–46}

Two-Step SARP to Prepare Highly Vibrating and Rotating Molecules. As discussed earlier, the efficiency of SARP population transfer relies on a strong two-photon Rabi frequency and a slow Stark-induced sweeping of the two-photon

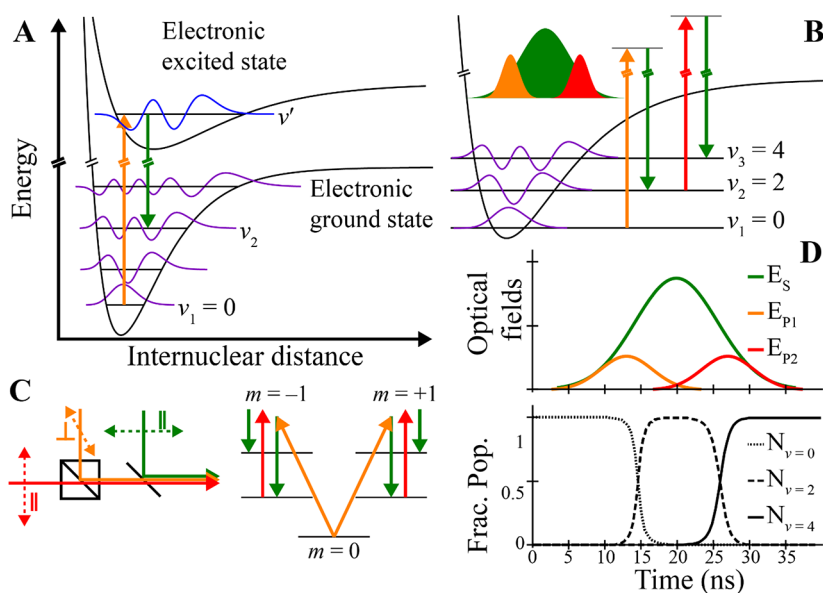


Figure 10. Two-step SARP process. (A) Raman excitation schematic, showing the wave functions of the initial and final states connected via an electronically excited vibronic state. The figure shows a resonant Raman transition for ease of illustration, but the SARP processes in this work involve off-resonant Raman transitions with virtual electronically excited vibronic states. The overlap between initial and final vibrational levels decreases with increasing change in vibrational quantum number. (B) Schematic of the two-step SARP process described in this Perspective. D_2 molecules are excited from the ($v=0$) ground state into the ($v=4$) target state using a sequence of two SARP processes that drives the population through a real intermediate ($v=2$) state. The inset shows the temporal pulse sequence, with a stronger Stokes pulse (1064 nm, 10 ns, green) partially overlapping with two weaker pump pulses (655 and 660–680 nm, 5 ns, orange and red). (C) Experimental arrangement for the combination of three laser pulses. The two pump pulses are combined using a polarizing cube, requiring that their polarizations be perpendicular to one another. As shown in the schematic, this produces the ($m = \pm 1$) state. (D) Theoretical simulation of the two-step SARP process shows the possibility of transferring the complete population to the final state, with no population left stranded in the intermediate state. Figure adapted from ref 96. Copyright 2022 American Chemical Society.

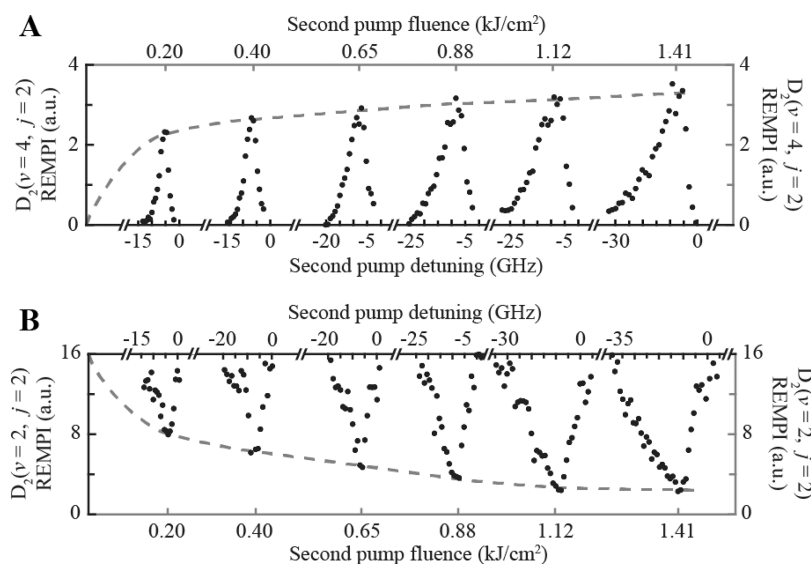


Figure 11. Saturation of the REMPI signal from the target state with its accompanying depletion from the intermediate state confirms the near-complete population transfer. Spectra of the second SARP step $D_2(v=2, j=2, m=\pm 1) \rightarrow D_2(v=4, j=2, m=\pm 1)$ as a function of the second pump laser fluence. The fluence and frequency of the first pump are held constant at values corresponding to the maximum population transfer. (A) Measured $D_2(v=4, j=2)$ target state REMPI signal. The saturation behavior of the signal with increasing pump fluence shows the threshold characteristic of the SARP process, demonstrating that the complete population transfer is achieved as long as the two-photon coupling is sufficiently strong to satisfy the adiabatic condition. (B) Depletion of the REMPI signal from the $D_2(v=2, j=2)$ intermediate state confirms complete population transfer. About 90% of the intermediate state molecules are pumped into the excited state within the measured REMPI volume. Figure reprinted from ref 96. Copyright 2022 American Chemical Society.

detuning that satisfies the adiabatic condition $d\Delta/dt \ll 4\Omega_R^2$ (eq 6). The two-photon Rabi frequency Ω_R is proportional to the Raman polarizability r_{12} (eq 2), and the Stark-induced detuning Δ is proportional to the difference optical polarizability

α_{12} between the initial state and the target state (eq 3). As mentioned earlier, the strength of the Raman coupling r_{12} depends on the overlap of the vibrational wave functions between the initial and target states. The decrease of r_{12} and the

simultaneous increase of α_{12} with increasing vibrational quantum number ν of the target state makes it increasingly difficult to satisfy the Landau–Zener condition and achieve a strongly avoided crossing that allows successful population transfer. Moreover, because of the large optical Stark shift of the rotationally aligned molecule, it becomes additionally difficult to satisfy SARP's adiabatic condition to prepare a rotationally aligned high vibrational state. We note that the orientation of the rotational angular momentum vector j provides the handle to control the collision geometry. Although in some instances using a single-step SARP may have been possible for transfer of the population to a rotationless ($j = 0$) high vibrational state ($\nu = 4$ and 7), SARP's adiabaticity condition could be fulfilled only over a small target volume. We note that a large target population is essential to obtain a good signal-to-noise ratio in the measurement of a state-resolved differential cross section, especially for collisions that involve neutral H_2 in the electronic ground state.

To overcome this limitation, a multicolor ladder SARP that connects the ground vibrational state to a highly excited vibrational state via one or more Raman-coupled intermediate states within the ground electronic surface was proposed⁴¹ (Figure 10). For each smaller $\Delta\nu$ SARP step, the adiabaticity condition is fulfilled because of the strong Raman coupling that results from the superior overlap of the vibrational wave functions of nearby vibrational states. The simulation of a two-step SARP process in Figure 10D shows that at the end of excitation complete population of the initial state (ν_1) is transferred to the target state (ν_3), leaving no population in the intermediate SARP state (ν_2). Recently, a two-step SARP transferring a large population from the ground state ($\nu = 0, j = 0$) to the rovibrationally excited states ($\nu = 4, j = 2$) and ($\nu = 4, j = 4$) of the deuterium molecule has been demonstrated.⁹⁶ The two sequential SARP steps were connected via the intermediate two-photon resonant D_2 ($\nu = 2, j = 2$) state. To achieve population transfer using the two-step SARP, a strong Stokes pulse was combined with a pair of weaker and delayed pump pulses, as illustrated in Figure 10B. The near-complete population transfer from the initial ($\nu = 0, j = 0$) state to either of the ($\nu = 4$) target states is demonstrated by the threshold behavior of the measured target population against the fluence of the pump lasers (Figure 11A). The complete population transfer is further supported by measuring the near-complete depletion of the population in the intermediate ($\nu = 2$) state (Figure 11B).

SARP Offers Coherent Stereodynamic Control by Preparing m -State Superposition. As mentioned in the beginning, stereodynamics plays an important role in controlling the outcome of a collision.^{15,25,29,30,97–101} Field-free stereodynamic control is essential for probing the 3D anisotropic molecular potentials. Through exploitation of the angular momentum selection rules for optical transition, SARP can prepare a target molecule in a single or a superposition of the magnetic sublevels m within a rovibrational eigenstate (ν, j), as such providing field-free control of the molecular frame. The m -state selection is accomplished by combining appropriate polarization directions of the pump and Stokes lasers optical fields. Figure 12 shows how SARP aligns the bond axis of the diatom (X_2) in the rotational state $j = 2$ along an arbitrary angle, α , with respect to the Z axis using parallel pump and Stokes optical fields polarized in the direction α . The SARP excitation scheme is also shown, where the projection m' of $j = 2$ refers to the Z' axis along α . The state of the polarized bond axis can be expressed as

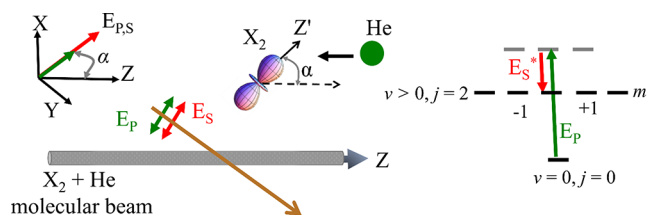


Figure 12. SARP control of bond-axis alignment using polarized pump and Stokes laser fields E_p and E_s . To align the bond axis along an arbitrary direction (Z') defined by the angle α relative to the Z axis, the pump and Stokes laser are combined with polarizations parallel to the direction α . The m and m' refer to the projections of the rotational angular momentum vector j along the quantization axis Z and Z' , respectively.

$$|\psi_\alpha\rangle = |\nu, j = 2, m' = 0\rangle = \sum_m d_{0m}^{j=2}(\alpha) |\nu, j = 2, m\rangle \quad (7)$$

In eq 7, $d_{0m}^{j=2}(\alpha)$ gives the Wigner rotation matrix for the angular momentum $j = 2$. SARP's ability to precisely define the molecular bond axis provides control over the collision geometry at the quantum level. Using two-step SARP, we are now able to polarize the bond axis in the ($\nu = 4, j = 4$) state. When different polarization states of the pump and Stokes optical fields are mixed, various m -state superpositions and coherent controls can be obtained for molecular scattering. For example, when right and left circularly polarized pump and Stokes laser pulses are mixed, SARP transfers the population to a single $m' = 2$ or -2 state of $j = 2$, where m' refers to a quantization axis along the laser beam propagation. In this state the bond axis is set to rotate like a cartwheel in a direction perpendicular to the collision velocity.

In general, for a SARP-prepared superposition state $\sum_m C_m |vjm\rangle$, the differential scattering cross section for the rotationally inelastic collision ($\nu, j \rightarrow \nu, j'$) can be expressed as follows:

$$\left(\frac{d\sigma}{d\Omega}\right)_{j \rightarrow j'} = \sum_{m'} \left| \sum_m C_m q_{jm \rightarrow j'm'} \right|^2 \quad (8)$$

In eq 8, C_m gives the amplitude of the m state in the SARP-prepared superposition, and $q_{jm \rightarrow j'm'}$ represents the amplitude for scattering from the initial (ν, j, m) to the final (ν, j', m') state within a differential solid angle $d\Omega$ defined in a laboratory fixed reference frame. The final scattered state (j', m') results from the interference of the various m states of the superposition defining the target state. The sum over m' implies that the polarization of the rotationally relaxed j' state is not measured, which is generally the case for the rotationally inelastic collision of H_2 . The interference can be seen more explicitly by expanding the differential cross section as follows:

$$\begin{aligned} \left(\frac{d\sigma}{d\Omega}\right)_{j \rightarrow j'} &= \sum_m |C_m|^2 \sum_{m'} |q_{jm \rightarrow j'm'}|^2 \\ &+ \sum_{m \neq n} C_m C_n^* \sum_{m'} q_{jn \rightarrow j'm'}^* q_{jm \rightarrow j'm'} \end{aligned} \quad (9)$$

In eq 9, the first term gives contributions from the individual m states with $|C_m|^2$ giving the m -state population within the superposition. The second term describes interference that results from different m states, with $C_m C_n^*$ giving coherence between the two sublevels m and n within the rotational state j .

For polarizing the bond axis at an angle α , we have $|C_m|^2 = |d_{0m}^i(\alpha)|^2$ and $C_m C_n^* = d_{0m}^i(\alpha) d_{0n}^i(\alpha)^*$, showing how SARP coherently controls the outcome of a scattering by controlling the polarization angle α of the pump and Stokes optical fields. The fine stereodynamic control offered by SARP is essential for measuring the vector correlations. Moreover, because the coherent superposition of the degenerate m states is stationary in time, it can be used to coherently control a bimolecular reaction. Some of these controls have already been demonstrated in the cold scattering experiments and also have been discussed theoretically.^{16–21,97,100,102}

Figure 13A,B show two specific collision geometries obtained by setting the polarization angle $\alpha = 0$ (HSARP, Figure 13A) and

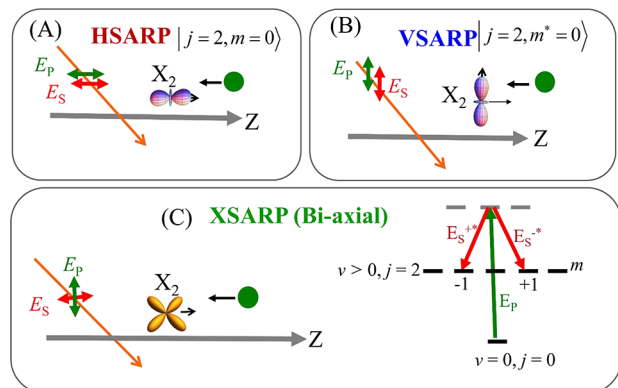


Figure 13. Three bond-axis alignments HSARP, VSARP, and XSARP by combining the polarizations of SRAP's pump and Stokes laser pulses. (A) HSARP is produced by combining the pump and Stokes optical fields polarized along the Z axis ($\alpha = 0$). (B) VSARP alignment is generated by the pump and Stokes fields polarized perpendicular to the Z axis ($\alpha = \pi/2$). In the HSARP state, the molecular bond axis is preferentially aligned parallel to the collision velocity, whereas in VSARP it is aligned perpendicularly. (C) XSARP is a biaxial state, produced by combining cross-polarized pump and Stokes laser pulses; the excitation schematic of XSARP is also shown on the right. In the XSARP state the bond axis simultaneously occupies two orthogonal orientations.

$\alpha = \pi/2$ (VSARP, Figure 13B). For the HSARP case the molecular bond axis is preferentially aligned along the collision

velocity, whereas for the VSARP case the bond axis is preferentially aligned perpendicular to the collision velocity. Figure 13C describes a special alignment or collision geometry (XSARP), which is achieved by combining the cross-polarized pump and Stokes laser pulses. The excitation schematic for preparing the XSARP state shows that it is a coherent superposition of $m = \pm 1$ state within the $j = 2$ state. The XSARP state is also called the biaxial state, which has a nonclassical feature because the bond axis simultaneously occupies two possible orientations in space, and thus acts exactly like a double slit for the coherent scattering of molecules. In the chosen system of coordinates with the quantization axis Z oriented parallel to the molecular beam propagation, HSARP, VSARP, and XSARP states can be expressed as follows:^{16–19}

$$|\text{HSARP}\rangle = |v, j = 2, m = 0\rangle \quad (10a)$$

$$|\text{VSARP}\rangle = -\frac{1}{2}|v, j = 2, m = 0\rangle + \sqrt{\frac{3}{8}}[|v, j = 2, m = 2\rangle + |v, j = 2, m = -2\rangle] \quad (10b)$$

$$|\text{XSARP}\rangle = \frac{|j = 2, m = 1\rangle - |j = 2, m = -1\rangle}{\sqrt{2}} \quad (10c)$$

As we will see later in the section “Experimental Study of Cold $j = 2 \rightarrow j' = 1$ and $j = 2 \rightarrow j' = 0$ Rotational Relaxations”, the scattering distribution and integral cross sections vary dramatically for the three collision geometries defined by HSARP, VSARP, and XSARP states. For the two-step SARP process (Figure 10), the bond-axis polarization is accomplished by delayed switching of Pockel's cell, which controls the relative polarizations of the optical fields in the three-pulse sequence as shown by the schematic in Figure 14.

METHOD OF PARTIAL WAVE ANALYSIS FOR THE ROTATIONALLY INELASTIC COLD SCATTERING EXPERIMENTS

Rotationally inelastic scattering can sensitively and non-invasively probe the anisotropic part of the van der Waals interactions. Through precise control of the internal quantum

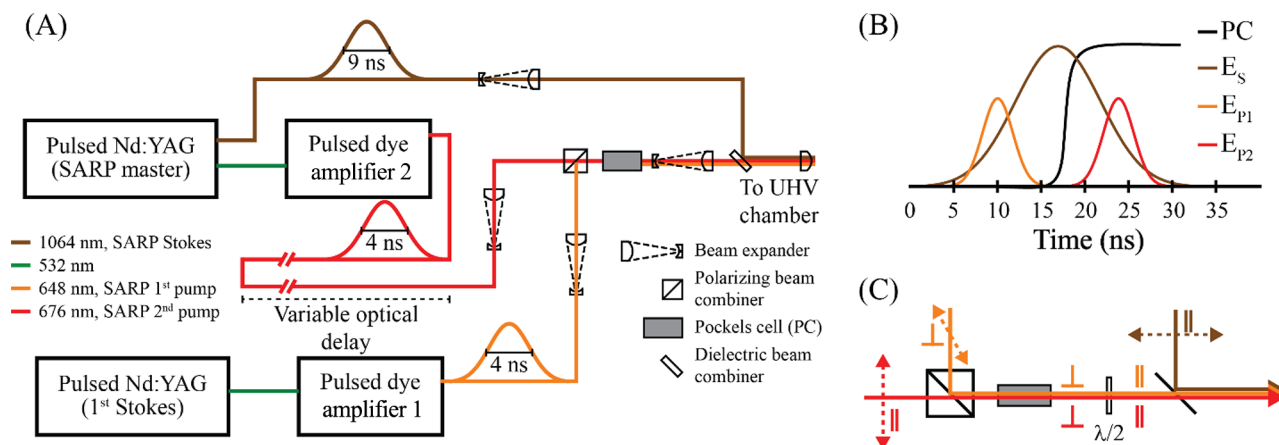


Figure 14. Bond-axis polarization in the two-step SARP process. (A) Experimental arrangement of the two-step SARP by combining a strong Stokes pulse (E_S , brown) with two weaker pump pulses (E_{P1} , orange, and E_{P2} , red). (B) The temporal sequence of the three laser pulses and switching voltage of Pockel's cell that rotates only the polarization of the delayed pump pulse (E_{P2}) by 90° . (C) Pockel's cell is followed by a half-wave plate that further rotates the polarizations of the two pumps relative to the Stokes pulse polarization, achieving the desired control of the bond-axis alignment.

state and alignment of the bond axis of H_2 molecules using SARP, a series of rotationally inelastic cold scattering (νj) \rightarrow ($\nu' j'$) experiments are carried out in our laboratory within a single co-expanded mixed molecular beam, as shown schematically in Figure 2 and Figure 3. This arrangement brings the collision temperature down to a few degrees Kelvin, allowing only a few low lying ($l = 0, 1, 2, 3$) incoming orbitals to contribute to the collision. The scattering angular distribution is generated by the interference of a set of outgoing orbitals that arise from the scattering of the few incoming orbitals. In the presence of a scattering resonance, the outgoing orbitals arise from a single incoming orbital that dominates the scattering process and leaves its signature in the angular distribution. A partial wave analysis has been developed for the angular distribution to extract information about the dynamics of resonant scattering.^{16–19} The analysis uses a set of selection rules connecting the incoming and outgoing orbitals that are based on the conservation of angular momentum and parity. In the following we discuss the orbital selection rules for the $\Delta j = 1$ and $\Delta j = 2$ rotational relaxations and give the basic guidelines of the partial wave analysis.

Orbital Selection Rules for the Rotationally Inelastic ($j \rightarrow j'$) Cold Collision. The atom–diatom interaction (between X_2 and B in Figure 15) can be expressed as^{1,89,91,103,104}

$$U(r, r', \gamma) = U_0(r, r') + \sum_{n=1}^{\infty} U_n(r, r') \sum_{k=-n}^n Y_{nk}^*(\theta', \varphi') Y_{nk}(\theta, \varphi) \quad (11)$$

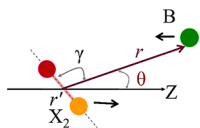


Figure 15. Atom–diatom anisotropic van der Waals interaction. The quantization Z axis is oriented along the relative velocity of the colliding species. θ gives the polar angle of the position vector r that connects the center of mass of the colliding atom B with the center of mass of the diatom X_2 . γ gives the angle between the bond axis of X_2 and the vector r . r' gives the bond length of the vibrationally excited diatom X_2 .

In eq 11, (r', θ', φ') defines the orientation of the molecular bond axis with respect to the quantization Z axis along the collision velocity, whereas (r, θ, φ) defines the relative position vector r connecting the center of mass of the two colliding species. $Y_{nk}(\theta', \varphi')$ and $Y_{nk}(\theta, \varphi)$ are the spherical harmonics of order n describing the anisotropy of the interaction potential that couples the rotational and translational degrees of freedom. For the homonuclear molecules only, even n values are allowed by the requirement of exchange symmetry. Keeping only the first three lowest order terms in the atom–diatom potential, we get

$$U = U_0(r, r') + U_1(r, r') \sum_{k=-1}^1 Y_{1k}^*(\theta', \varphi') Y_{1k}(\theta, \varphi) + U_2(r, r') \sum_{k=-2}^2 Y_{2k}^*(\theta', \varphi') Y_{2k}(\theta, \varphi) \quad (12)$$

The isotropic $U_0(r, r')$ part generates the attractive force in the radial direction and does not mix the rotational states. The $\Delta j = 1$ transition is exclusively driven by the first anisotropic term

proportional to $U_1(r, r')$ and gives rise to the orbital selection rule $\Delta l = l - l' = \pm 1$, where l and l' represent the incoming and outgoing orbitals, respectively. The second anisotropic term proportional to $U_2(r, r')$ drives the $\Delta j = 2$ transition, giving rise to the selection rule $\Delta l = 0, \pm 2$ for the orbitals. For the diatom–diatom interactions, there is an additional third term that describes coupling between two rotating molecules. For example, the $\Delta j = 2$ transition for homonuclear diatom–diatom collision, the interaction can be expressed as

$$U = U_0(r, r_1, r_2) + U_{202}(r, r_1, r_2) \sum_{m=-2}^2 Y_{2m}^*(\theta_1, \phi_1) Y_{00}(\theta_2, \phi_2) Y_{2m}(\theta, \phi) + U_{224}(r, r_1, r_2) \sum_{\substack{m_1, m_2, m \\ m=m_1+m_2}} Y_{2m_1}^*(\theta_1, \phi_1) Y_{2m_2}(\theta_2, \phi_2) Y_{4m}(\theta, \phi) \quad (13)$$

The second term, proportional to U_{202} , in eq 13 describes the anisotropic interaction that drives the $\Delta j = 2$ transition in one of the pairs, whereas the partner molecule is left unchanged. This interaction is similar to that of the atom–diatom anisotropic term proportional to the potential $U_2(r, r')$ in eq 12, giving rise to the orbital selection rules $\Delta l = 0, \pm 2$. The third term, proportional to U_{224} , couples the two rotating molecules, generating the selection rules $\Delta l = 0, \pm 2, \pm 4$ for the orbitals. This term is responsible for changing the state of both partners including the reorientation of their angular momentum. These orbital selection rules are used to develop the partial wave analysis for the measured scattering angular distribution.

Partial Wave Analysis. Figure 16 schematically describes the experimental arrangement for measuring the center-of-mass

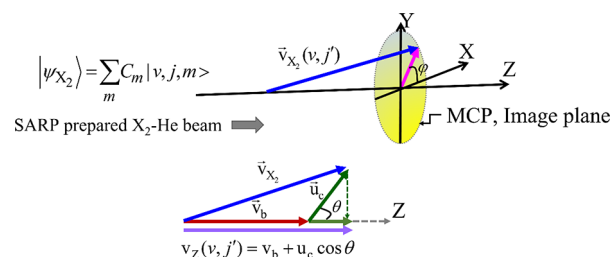


Figure 16. For cold scattering within a well-collimated mixed molecular beam, the center of mass scattering angles (θ, φ) are defined relative to the Z axis oriented along the relative velocity of the partner molecules. $\vec{v}_{X_2}(v, j')$ is the lab-frame velocity of the inelastically scattered product, $\vec{v}_{X_2}(v, j') = \vec{u}_c(v, j') + \vec{v}_b$, where \vec{u}_c is the center of mass velocity of the product, and \vec{v}_b is the lab-frame peak velocity of the unscattered molecular beam along the Z axis. The projection v_z of $\vec{v}_{X_2}(v, j')$ on to the Z axis determines the center-of-mass polar angle θ from the time-of-flight measurement of the product ions. $\cos \theta = (t_b - t_s/Su_c)$, where t_b and t_s are the time-of-flights of the unscattered (v, j) and scattered (v, j') X_2 , respectively, and S is a calibration parameter of the ionization mass spectrometer. In the experiments discussed here, the differential scattering angular distribution is averaged over the azimuthal angle φ .

angular distribution in a co-expanded mixed beam with the 1D relative velocity along the Z axis. Before discussion of specific cold scattering experiments, it is pertinent to describe the basic principles underlying the partial wave analysis. Let us consider the rotationally inelastic scattering where the initially prepared molecule in the $(\nu_1 j_1)$ state relaxes into the final $(\nu_1 j_1')$ state via collision with another species having angular momentum j_2 . In

the following analysis we focus our attention only on those collisions where the partner molecule in the j_2 state does not relax to another rotational state, a condition that can be validated experimentally by using conservation of the total energy. The state-to-state differential scattering amplitude for the rotational relaxation ($j_1 m_1 \rightarrow j_1' m_1'$) of the target molecule can be expanded as the coherent superposition of the various outgoing orbitals or partial waves ($l' m_l'$):

$$q_{j_1 m_1 \rightarrow j_1' m_1'}(\theta, \varphi) = \sum_{J, l, l'} A_{l' m_l'}(j_1 m_1 l m_l; JM) Y_{l' m_l'}(\theta, \varphi) \quad (14)$$

$q_{j_1 m_1 \rightarrow j_1' m_1'}$ represents the state-to-state scattering amplitude within a differential solid angle $d\Omega$ in the direction defined by the center of mass polar angle (θ) and the azimuthal angle (φ) relative to the Z axis, as pictured in Figure 16. In eq 14 $Y_{l' m_l'}(\theta, \varphi)$ represents the outgoing scattered orbitals ($l' m_l'$). $A_{l' m_l'}(j_1 m_1 l m_l; JM)$ gives the amplitude for scattering of a single incoming state, defined by the internal and orbital angular momentum quantum numbers ($j_1 m_1; l m_l$), into the outgoing state ($j_1' m_1'; l' m_l'$) for a given total angular momentum J and its projection M along the Z axis. $A_{l' m_l'}(j_1 m_1 l m_l; JM)$ results from the product of the relevant scattering matrix and the Clebsch-Gordan (CG) coefficients for coupling of the internal angular momentum, with the orbital angular momentum producing the total angular momentum J . Exact expression for the expansion coefficients for specific collisions can be found elsewhere.^{58,77,105,106} The outgoing orbitals ($l' m_l'$) are determined using the conservation of the angular momentum and parity as mentioned earlier. In each collision event the total angular momentum J and its projection M must be conserved, satisfying $J = j_1 + j_2 + l = j_1' + j_2' + l'$ and $M = m_1 + m_2 + m_l = m_1' + m_2' + m_l'$, where m_1 , m_2 , and m_l give the projection quantum numbers for the internal and orbital angular momenta j_1 , j_2 , and l on to the quantization Z axis, and similarly, m_1' , m_2' , and m_l' refer to the projection quantum numbers for the scattered channels. Further simplification is achieved by choosing the quantization Z axis along the collision velocity, which coincides with the direction of the mixed-beam propagation. Because the orbital angular momentum vector l cannot have any projection on the relative velocity along the Z axis, we have $m_l = 0$. With use of the conservation of angular momentum, this leads to $m_l' = (m_1 + m_2) - (m_1' + m_2')$. Additional simplification is possible when the partner molecule is not reoriented in the collision process, giving $m_2' = m_2$ and $m_l' = m_1 - m_1'$. Likewise, for collision between the diatom and a spinless atom with $j_2 = j_2' = 0$, we have $m_l' = m_1 - m_1'$. As such, the atom-diatom rotationally inelastic collision can be simplified, giving¹⁰⁶

$$A_{l' m_l'}(j_1 m_1 0; JM) \propto \langle j_1 l m_1 0 | j_1 l J M \rangle \times \langle j_1' l' m_1' m_l' | j_1' l' J M \rangle \times S^J(j_1; j_1')$$

where $S^J(j_1; j_1')$ gives the scattering matrix for the inelastic $j \rightarrow j'$ transition, and $\langle j_1 l m_1 0 | j_1 l J M \rangle$ gives the CG coefficient for coupling of the angular momentum j and l producing the total angular momentum J . The CG coefficients gives the geometric factor, whereas the scattering matrix S contains information about the dynamics.

With the well-defined angular momentum projection m_1 in the incoming channel, the interference of a small number of outgoing orbitals ($l' m_l'$) produces sharply defined structures in the scattering angular distribution. In the presence of a scattering resonance these features can be identified as originating from a

specific incoming orbital that dominates the collision. In our inelastic scattering experiments SARP selects the specific m states for the incoming channel, whereas the projection m' for the outgoing scattered states (j', m') are not measured. Because the scattering is not resolved with respect to the azimuthal angle φ , the measured angular distribution in polar angle θ is obtained by integrating the differential cross section over the azimuthal angle φ , that is,

$$\left(\frac{d\sigma}{d\theta} \right)_{j \rightarrow j'} = \sin \theta \int_0^{2\pi} \left(\frac{d\sigma}{d\Omega} \right)_{j \rightarrow j'} d\varphi \quad (15)$$

Using eq 8 in eq 15 and replacing the state-to-state scattering amplitude $q_{j_1 m_1 \rightarrow j_1' m_1'}$ with its partial wave expansion given in eq 14, we get an integral expression for $(d\sigma/d\theta)_{j \rightarrow j'}$ in terms of the outgoing orbitals $Y_{l' m_l'}(\theta, \varphi)$, which is then fitted to the measured angular distribution. With a very small number of orbitals in the incoming channel together with a precisely defined internal state, the partial wave fit to the angular distribution reliably generates the relative contributions of the outgoing orbitals. The detailed dynamics of the collision is revealed by relating each outgoing orbital with the orbitals in the incoming channel. In favorable cases it may be possible to extract the scattering matrix from the fitting parameters. The implications of the partial wave analysis will become clear as we discuss the various cold scattering experiments.

EXPERIMENTAL STUDY OF COLD $j = 2 \rightarrow j' = 1$ AND $j = 2 \rightarrow j' = 0$ ROTATIONAL RELAXATIONS

The rotationally inelastic cold collisions of HD and D₂ have been studied by preparing them in rovibrationally excited ($v = 1, 2, j = 2$) and aligned target states using SARP.^{16,17,19–21,80} These experiments studied the rotational relaxations, $j = 2 \rightarrow j' = 1$ and $j = 2 \rightarrow j' = 0$ mediated by either a He atom or a H₂ or D₂ molecule co-expanded with the target in a single molecular beam. In each case the concentration of the target molecules in the gas mixture was appropriately diluted to avoid collisions between a pair of target species, so that measured scattering arises exclusively from the collision with its partner. In these experiments the state of the partner has been left unprepared. With precise control of the initial target state combined with the state-selective detection of the collision product, the low-temperature collision in a directed beam allowed a detailed partial wave analysis of the scattering angular distributions, revealing the dynamic nature of quantum interactions. With use of this analysis, it was possible to identify a single resonant orbital in the incoming channel that dominated the cold scattering. Parallely, a great deal of theoretical work targeting these quanta-controlled scattering experiments that have led to deeper understanding of the collision dynamics has been developed.^{58,100,107,108} In the following we discuss some of these cold scattering experiments.

Four-Vector Correlation Measured in the $j = 2 \rightarrow j' = 1$ Relaxation of HD with D₂.¹⁶ The study of the stereodynamics provides insight into the anisotropic molecular interactions. The four-vector correlation $\mathbf{k} - \mathbf{j} - \mathbf{k}' - \mathbf{j}'$, where \mathbf{k} and \mathbf{k}' are the initial and final relative velocities and \mathbf{j} and \mathbf{j}' are the initial and final rotational angular momentum vectors of the quantum-state-prepared reactant, best quantifies the stereodynamics of a collision. By preparing HD in specific rovibrationally excited and aligned ($v = 1, j = 2, m$) target states, the ($v = 1, j = 2$) \rightarrow ($v = 1, j' = 1$) rotational relaxation via cold collision with unprepared D₂ molecules was studied by co-expanding the partners in a single

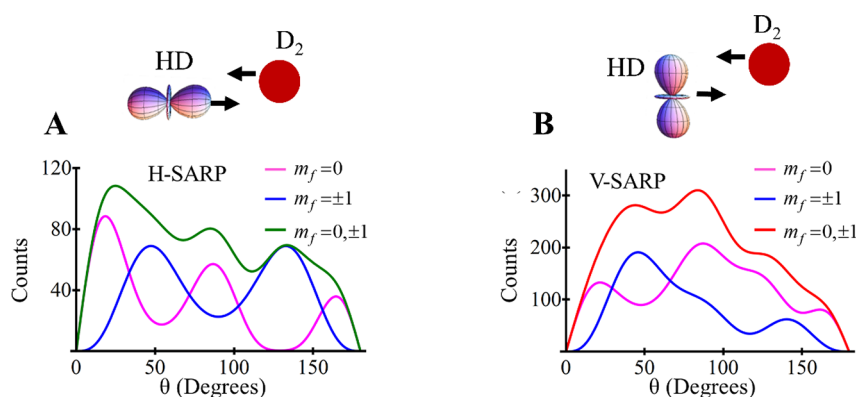


Figure 17. Polarization of the final scattered product in rotationally inelastic collision of state-prepared HD ($\nu = 2, j = 2$) with unprepared D_2 molecules in a mixed supersonic beam. Angular distribution ($d\sigma/d\theta$) $_{j=1, m_f}$ of the scattered HD ($\nu = 1, j' = 1$) with specific orientations defined by the projection quantum number m_f of the final angular momentum vector j' on to the Z axis for the HSARP and VSARP alignments of the HD bond axis. (A) Scattering angular distributions for different polarizations of the product state HD ($\nu = 1, j' = 1$) for the initial HD bond axis aligned parallel to the molecular beam axis (HSARP). (B) Scattering angular distribution for different polarizations of the product state HD ($\nu = 1, j' = 1$) for the initial HD bond axis aligned perpendicular to the molecular beam axis (VSARP). Curves labeled $m_f = 0, \pm 1$ in each plot give the theoretical scattering distribution obtained by partial wave fit to the experimental angular distribution. Angular distributions for specific outgoing angular momentum polarization are given by the blue and magenta curves. The green (HSARP) and the red (VSARP) give the angular distribution for the total (unpolarized product). Figure adapted from ref 16. Copyright 2017 The American Association for the Advancement of Science.

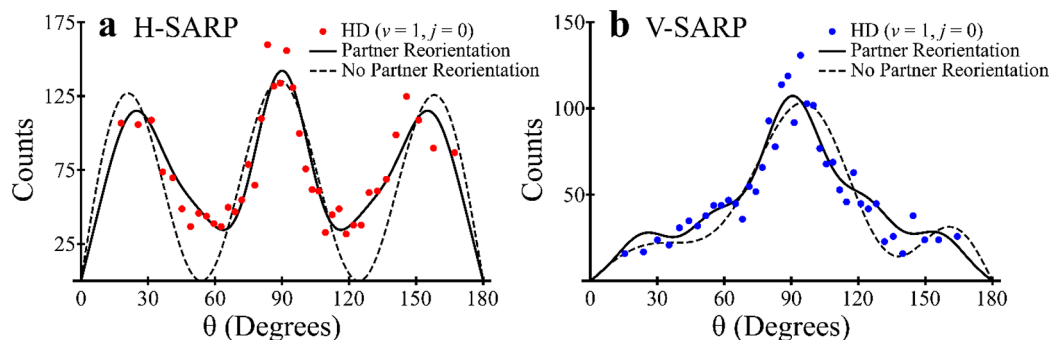


Figure 18. H_2/HD mixed beam scattering. Partner reorientation revealed by partial wave analysis of the HD- H_2 cold scattering at the collision energy of ~ 2 K. Partial wave fit to the measured angular distribution for the $\Delta j = 2$ rotationally inelastic collisions of state-prepared HD ($\nu = 1, j = 2$) with unprepared H_2 for the HD bond axis preferentially aligned (a) parallel (HSARP) and (b) perpendicular (VSARP) to the relative velocity between HD and H_2 . The red (a) and blue (b) points show the experimental angular distribution of the scattered HD ($\nu = 1, j' = 0$) derived from the time-of-flight measurements of REMPI-generated ions. In both (a) and (b), the dashed curves give partial wave fits generated using functions that neglected H_2 reorientation, and the solid curves give partial wave fits generated using functions that included H_2 reorientation. The strong HSARP scattering accompanying partner reorientation suggests involvement of the o - H_2 . Figure adapted from ref 17. Copyright 2018 Springer Nature.

supersonic beam. The scattering angular distribution was measured for the HSARP and VSARP orientations of the HD ($\nu = 1, j = 2$) target state. The partial wave analysis of the rotationally relaxed product HD ($\nu' = 1, j' = 1$) angular distribution yielded the four-vector correlations between $\mathbf{k}, \mathbf{j}, \mathbf{k}'$, and \mathbf{j}' (see Figure 17).¹⁶ Figure 17 shows the fitted angular distributions for the different orientations ($m_f = 0, \pm 1$) of the angular momentum vector j' of the scattered HD ($\nu = 1, j' = 1$). The angular distributions for the polarized product states were extracted using the partial wave fit to the measured distributions.

Partner Reorientation in the Resonant Dynamics of $j = 2 \rightarrow j' = 0$ Relaxation.¹⁷ The cold collision combined with SARP's ability to select a single internal quantum state captures the dynamics at the limit of a single partial wave and provides the deepest insight of the mechanism of molecular interaction. The rotational relaxation of HD ($\nu = 1, j = 2$) \rightarrow HD ($\nu' = 1, j' = 0$) via cold collision with unprepared D_2 and H_2 was studied by preparing the HSARP and VSARP bond-axis alignments of HD. The partial wave analysis of the scattering angular distribution revealed that the rotational relaxation proceeds through the

simultaneous reorientation of the partner molecule (Figure 18). This suggests that the strong scattering observed with H_2 as the collision partner is driven mainly by the o - H_2 ($\nu = 0, j = 1$). Besides demonstration of a strong stereodynamic preference for the $\Delta j = 2$ inelastic scattering, the partial wave analysis was able to extract the dominant anisotropies that include a strong short-range and a relatively weaker long-range potential term resulting from the quadrupole–quadrupole interactions between a pair of rotating molecules as described in the section “Method of Partial Wave Analysis for the Rotationally Inelastic Cold Scattering Experiments”. The partial wave analysis also suggested the footprint of a shape resonance for collision with H_2 , which was later confirmed with high-level quantum scattering calculations.^{17,58} Theory was able to successfully reproduce experimental angular distribution that results mainly from the $l = 2$ shape resonance in agreement with the partial wave fit.

Stereodynamic Preference in Resonant Collision of HD and He.¹⁹ It is well-known that by polarizing the reactants, one controls the reaction products. Because the quantum state in the incoming channel can be fully defined for the atom–diatom

collision, it allows us to study how the product channels are determined by the initial polarization of the target molecule. To study the steric effects in atom–diatom collisions, the HD was prepared in the rovibrational ($v = 1, j = 2$) state with its bond axis aligned in HSARP, VSARP, and XSARP orientations. The rotational relaxation HD ($v = 1, j = 2$) \rightarrow HD ($v' = 1, j' = 0$) via cold collision with He was studied within the co-expanded molecular beam of HD and He. The partial wave analysis of the product HD ($v' = 1, j' = 0$) angular distribution revealed how the inelastic scattering rate depends upon the initial orientation or m state of the target. The partial wave fit to the measured product angular distributions for different initial m states are reproduced in Figure 19, which clearly shows the stereodynamic preference

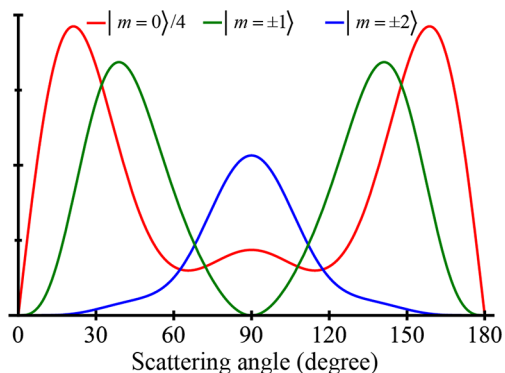


Figure 19. HD-He stereodynamics. The $\Delta j = 2$ rotationally inelastic HD-He scattering angular distribution $d\sigma/d\theta$ for different initial m states of the state-prepared HD ($v = 1, j = 2$). The red ($m = 0$), green ($m = \pm 1$), and blue ($m = \pm 2$) curves give the scattering angular distribution $d\sigma/d\theta$ calculated using the scattering matrix elements that are found from the partial wave fits to the measured HSARP and VSARP angular distribution of HD ($v = 1, j = 2, m$) \rightarrow ($v' = 1, j' = 0$) cold scattering. To bring the different scatterings in the same scale, the angular distribution of HD ($v = 1, j = 2, m = 0$) is divided by 4, showing that this state scatters most efficiently into the final ($v' = 1, j' = 0$) state. Figure adapted from ref 19. Copyright 2019 AIP Publishing.

of the HSARP ($m = 0$) alignment of HD over that of the $m = \pm 1$ and ± 2 states. SRAP's ability to fully control the collision geometry combined with the partial wave analysis in atom–diatom cold collision, thus, reveals the unprecedented details of the stereodynamics. Similar stereodynamic preferences have also been predicted by recent theoretical studies.¹⁰⁸

$l = 2$ Shape Resonance and Controversy of D_2 -He Cold Scattering.⁸⁰ The amount of information that can be obtained from a scattering experiment depends upon the precision with which the incoming channel is defined. The high level of precision achieved in the SARP-controlled atom–diatom cold collision opens the possibility to test the high-level theoretical calculations. The rotational relaxation of D_2 via collision with a He atom constitutes one of the simplest atom–diatom scattering experiments that disagreed with theory, raising concern about the accuracy of well-established H_2 -He interaction potential. The cold $j = 2 \rightarrow j' = 0$ rotational relaxation of D_2 ($v = 2, j = 2$) was studied within the mixed beam of D_2 and He for three specific bond-axis orientations HSARP, VSARP, and XSARP of D_2 . The partial wave analysis of the measured D_2 ($v = 2, j' = 0$) angular distribution revealed the dynamics of a resonant scattering that has the characteristic feature of a $l = 2$ shape resonance. Here, we present some details

of this analysis. The scattering angular distribution for the HSARP, VSARP, and XSARP alignments are expressed as

$$\left(\frac{d\sigma}{d\theta}\right)_H = \sin\theta \int_0^{2\pi} |q_{j=2, m=0 \rightarrow j'=0}|^2 d\varphi \quad (16)$$

$$\left(\frac{d\sigma}{d\theta}\right)_V = \sin\theta \int_0^{2\pi} \left| -\frac{1}{2}q_{j=2, m=0 \rightarrow j'=0} + \sqrt{\frac{3}{8}} [q_{j=2, m=2 \rightarrow j'=0} + q_{j=2, m=-2 \rightarrow j'=0}] \right|^2 d\varphi \quad (17)$$

and

$$\left(\frac{d\sigma}{d\theta}\right)_X = \sin\theta \int_0^{2\pi} \left| \sqrt{\frac{1}{2}}q_{j=2, m=1 \rightarrow j'=0} + \sqrt{\frac{1}{2}}q_{j=2, m=-1 \rightarrow j'=0} \right|^2 d\varphi \quad (18)$$

As discussed earlier, with use of conservation of the angular momentum along the Z axis, the state-to-state scattering amplitude $q_{j=2, m \rightarrow j' = 0}$ can be expanded in terms of outgoing partial waves:

$$q_{j=2, m \rightarrow j' = 0} = \sum_l c_l Y_{l, m}(\theta, \varphi) \quad (19)$$

The complex amplitudes c_l of the outgoing orbitals are determined by numerically fitting the integral expressions (eqs 16 and 17) to the measured HSARP and VSARP angular distributions. The numerical fitting procedure generates a set of self-consistent complex amplitudes c_l that produces a good fit to the HSARP and VSARP angular distributions with $R^2 > 0.99$. The amplitude and phase of the complex fitting parameters are further validated by calculating and showing that they also make a good fit to the XSARP angular distribution. Traveling in a single molecular beam, the colliding partners often have the overlapping velocity distributions with nearly coinciding peak velocities, like in the case of D_2 and He (Figure 2). As such, the cold scattering measured within a given solid angle is contributed by both positive and negative collision velocity groups, as pictured in Figure 20. The contributions from both

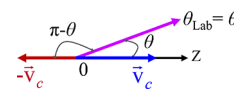


Figure 20. In a co-expanded mixed beam, the collision velocity distribution has both positive and negative velocity groups that contribute to the scattering measured at a laboratory angle $\theta_{\text{Lab}} = \theta$ relative to the Z axis. θ refers to the center of mass scattering angle. The contribution from the positive collision velocity group ($+v_c$) scattering at the angle θ is added to the contribution from the negative velocity group ($-v_c$) scattering at the angle $\pi - \theta$. The partial wave fit to the scattering distribution takes both contributions into account.

positive and negative velocity groups are included in the partial wave fit of the angular distributions using

$$I(\theta_{\text{Lab}} = \theta) \propto \left[\frac{d\sigma(\theta)}{d\theta} + \frac{d\sigma(\pi - \theta)}{d\theta} \right] \quad (20)$$

Figure 21A shows excellent fit to the HSARP and VSARP scattering angular distributions with even outgoing orbitals $l' =$

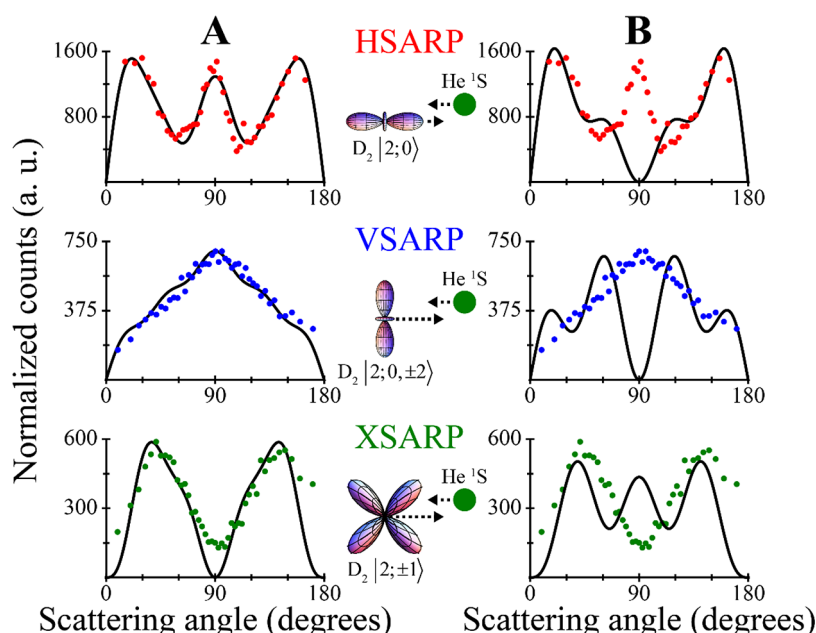


Figure 21. Fitting of measured angular distributions with even and odd outgoing orbitals. Colored dots give experimental data, whereas solid black curves give the results of our partial wave analysis, as described in the text. The images in the middle show the collision geometry in the center-of-mass frame for each of the bond-axis orientations: HSARP, VSARP, and XSARP. (A) HSARP and VSARP fit ($R^2 > 0.99$) with the even outgoing orbitals $l' = 0, 2, 4$. For XSARP, the black curve is calculated ($R^2 = 0.94$) using the complex fitting coefficients found from HSARP and VSARP fits. (B) HSARP, VSARP, and XSARP fit with odd $l' = 1, 3$ outgoing orbitals following the same procedure. Clearly, we are not able to fit the experimental data using these odd partial waves. Figure adapted from ref 18. Copyright 2021 AIP Publishing.

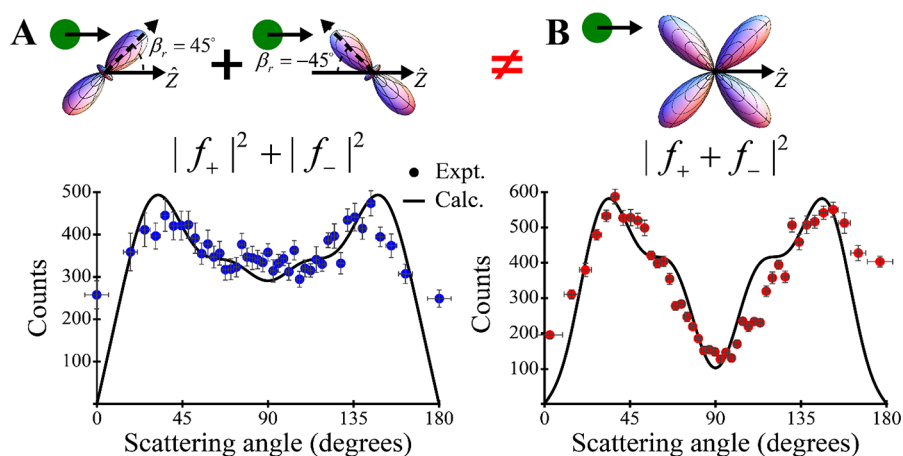


Figure 22. Demonstration of a quantum mechanical double slit by preparing the biaxial and uniaxial orientations of the bond axis of D_2 ($v = 2, j = 2$). (A) Experimental scattering distribution (blue dots) for the uniaxial bond axis orientation at $\beta_{\text{Lab}} = \pi/4$. This orientation generates angular distribution that is identical to the distribution measured with the bond axis oriented at $\beta_{\text{Lab}} = -\pi/4$. (B) Experimental scattering distribution (red dots) for the XSARP biaxial bond-axis orientation. The black solid lines in (A) and (B) show the calculated angular distributions using the scattering matrix, which were derived in earlier cold scattering experiments of D_2 and He. Vertical error bars represent the standard deviation in the number of counts at a given scattering angle, and the horizontal error bars give the experimental uncertainty in the determination of the scattering angle. The sum of the scattering distribution from the two uniaxial orientations is drastically different from the angular distribution from the biaxial states. The spectacular difference between the two scatterings arises because of the interference of the two uniaxial orientations, which are coherently coupled in the biaxial state and behave like the two mechanical slits in a traditional double slit. Figure reprinted from ref 20. Copyright 2021 The American Association for the Advancement of Science.

0, 2, 4 that arise exclusively from the incoming $l = 0, 2$, as suggested by the quadrupolar selection rules $\Delta l = 0, \pm 2$ (see section “Method of Partial Wave Analysis for the Rotationally Inelastic Cold Scattering Experiments”). The scattering matrix elements determined from the HSRAP and VSARP fits are used to calculate the XSARP distribution that produces an excellent fit to the experimental XSARP angular distribution shown in the bottom panel of Figure 21A. The failure to fit the angular

distribution using the odd outgoing waves $l' = 1, 3, 5$ (Figure 21B) shows that the $l = 1, 3$ incoming orbitals do not contribute to the scattering. The strongest amplitude of the $l' = 0$ orbital, which arises solely from the scattering of the incoming $l = 2$ orbital, suggests a possible $l = 2$ shape resonance that has a characteristic feature fingerprinted in the scattering angular distribution.

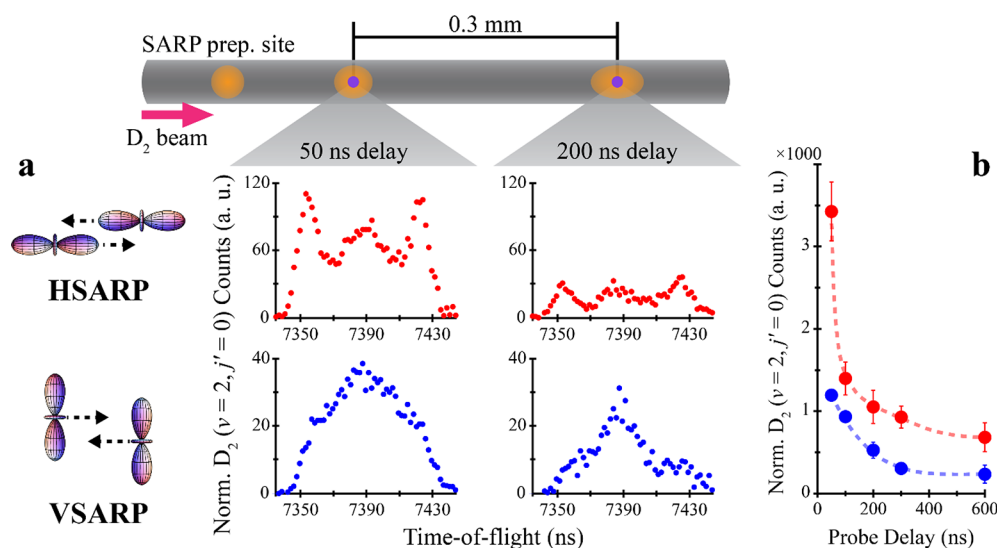


Figure 23. SARP's control of collision energy and stereodynamics for aligned–aligned collision between a pair of state-prepared D₂. HSARP and VSARP scattering rates change as we move the probe beam along the molecular beam propagation direction. Schematic at the top shows the SARP preparation of the molecular beam (orange spot, $\sim 100 \mu\text{m}$). As the delay is increased, this spot propagates downstream and spreads along the propagation direction. Scattering products generated within the small REMPI probe volume (purple spots, $\sim 20 \mu\text{m}$) are detected. (a) Measured time-of-flight distributions of scattered D₂ ($v = 2, j' = 0$) for the HSARP (red dots) and VSARP (blue dots) alignments at delays of 50 and 200 ns following SARP preparation. In these measurements, the delay and displacement of the REMPI laser are carefully matched to maximize the number of scattering products. In HSARP, the total number of counts drops by a factor of ~ 3.5 , whereas for VSARP it drops by a factor of ~ 2 as the delay is increased from 50 to 200 ns. (b) Relative HSARP and VSARP integral scattering rates as a function of SARP–REMPI delay in nanoseconds. The HSARP scattering rate drops dramatically as the delay increased from 50 to 600 ns, whereas the VSARP rate drops much more mildly, indicating the presence of a geometry-dependent collisional resonance. The dashed lines are only visual guides. Figure reprinted from ref 21. Copyright 2022 Springer Nature.

Recently, Jambrina et al.¹⁰⁷ studied this inelastic D₂-He collision theoretically using full dimensional close-coupling calculations with highly accurate interaction potential. Their study, however, indicates the presence of a much stronger $l = 1$ resonance that is accessible within the broad experimental D₂-He collision temperature shown in Figure 2. However, an effort to fit the experimental angular distribution with their theoretical calculations, which include contributions from the $l = 1$ resonance, failed. Jambrina et al. showed that the experimental data can be fit to the theory only when the contributions from the $l = 1$ incoming orbitals are completely ignored. The theoretical fit to the experimental data using only the even outgoing orbitals agrees with the earlier partial wave fit to the experimental angular distribution shown in Figure 21A. However, the complete absence of the strong $l = 1$ resonant orbital remains unexplained. The conflict between experiment and theory cannot be mitigated by considering a higher rate of collision present at the calculated temperature for the $l = 2$ resonance. This example illustrates that SARP provides the precision of quantum control that can be used to test a high-level scattering calculation.

SARP Prepares Quantum-Mechanical Double Slit to Coherently Control Molecular Scattering.²¹ As a direct consequence of the wave nature of matter, interactions at the quantum scale are often controlled by interference of indistinguishable quantum mechanical pathways connecting initial and final states. Historically, interference between two indistinguishable pathways in a double-slit experiment most conclusively demonstrated the wave properties of particles. In a quest to observe quantum interference in a two-body collision, a quantum mechanical double slit is realized by preparing D₂ ($v = 2, j = 2$) in a biaxial state using SARP, as illustrated in Figure 13C. The biaxial state has a nonclassical character because in this state

the bond axis of D₂ simultaneously occupies two possible orthogonal orientations that may act as two slits for the scattering of another particle. The density matrix representing such a state has nonzero off-diagonal elements that represent phase coherence between the two orientational states. The coherently coupled bond-axis orientations in the biaxial state led to the two indistinguishable pathways connecting the initial and final state for the $\Delta j = 2$ rotationally inelastic D₂-He scattering. The double-slit interference is manifested as a strong modulation in the measured angular distribution of the rotationally relaxed D₂ ($v = 2, j' = 0$) (Figure 22). Indeed, the coupled orientations within the biaxial state mimics the two mechanical slits in a traditional double-slit scattering experiment. To prove that the observed interference arose from the double-slit action of the biaxial state, the effect of one slit at a time must be measured separately. For this purpose, each of the uniaxial states (with bond axis aligned at $\alpha = \pm\pi/4$) contained within the superposition of the biaxial state was prepared by SARP (Figure 12). The scattering angular distributions measured for each slit, which is for each of the uniaxial states, shows remarkable difference from that of the biaxial state (Figure 22). This difference that clearly arises from the quantum mechanical interference of the two orientations of D₂ unequivocally establishes the double-slit action of the biaxial state. This experiment demonstrates that SARP provides the ability to experimentally engineer a quantum interferometer for controlling or measuring the fundamental properties of a molecular process. A higher level of control can be obtained by introducing a variable phase shift between the coherently coupled states, thus opening completely new possibilities for controlling a chemical reaction by changing the relative phase rather than the number density.

SARP Controls Collision Energy for Aligned–Aligned Bimolecular Collision. There is great interest in achieving a high level of stereodynamic control by preparing both reactants in specific aligned target states. Using a single-step SARP, we can control only one of the colliding species in a bimolecular collision. However, cold scattering can be studied between a pair of the same species in a pure beam prepared in a specific target state, thus opening the possibility of studying aligned–aligned scattering. Additionally, by preparation of quantum states at one location and probing at a different location along the molecular beam propagation, SARP can differentially control the velocity distribution or the collision energy between a pair of state-prepared molecules. The last control arises because of the dispersion of molecular beam velocities. To study the quantum mechanism of cold aligned–aligned scattering, the D_2 molecules within the molecular beam of pure D_2 were prepared in the rovibrationally excited ($v = 2, j = 2$) state with its bond axis aligned either in HSARP or VSARP orientations, thus defining two possible collision geometries as shown in Figure 23. The $\Delta j = 2$ rotationally inelastic scattering within the pure beam of D_2 has demonstrated the highly anisotropic character of aligned–aligned collision between a pair of SARP-aligned D_2 ($v = 2, j = 2$) molecules. The rotationally relaxed product D_2 ($v' = 2, j' = 0$) angular distribution was measured for each collision geometry by probing with REMPI at different distances from the SRAP preparation site. Figure 23a shows dramatically different differential scattering rates measured for the HSARP and VSARP geometries at two different probe locations along the molecular beam corresponding to the SARP–REMPI delays of 50 and 200 ns. Figure 23b shows that the integral scattering rate drops with the increase of SARP–REMPI delay for both HSARP and VSARP geometries. We should note that the $D_2(v = 0)$ molecules in $j = 1, 2$, which were not prepared by SARP, can also contribute to the observed scattering. The drop of the scattering rates, however, correlates only with the drop of the measured width of the collision velocity distribution between a pair of state-prepared D_2 . Measurement shows that the collision velocity distribution between the prepared and unprepared pair did not change with the distance or the delay, confirming that the observed scattering mainly arises from the aligned–aligned collision. The sharp drop of collision rates that correlates with the narrowing of collision velocity distribution suggested the presence of a shape resonance. The partial wave analysis confirmed this shape resonance, identifying the $l = 2$ as the dominant orbital contributing to the aligned–aligned scattering at the available collision temperature within the D_2 beam. Similar anisotropic dynamics in aligned–aligned scattering has also been observed with KRb molecules at ultracold temperature.⁶²

■ SARP OPENS NEW AVENUES TO EXPERIMENTALLY PROBE THE QUANTUM MECHANISM OF MOLECULAR INTERACTIONS

Combining SARP with the molecular beam methods provides a unique platform to control both the internal and external degrees of freedom of a two-body collision. Through various examples of rotationally inelastic cold scattering experiments, it is illustrated how SARP coherently controls the dynamics of anisotropic interactions by preparing quantum superpositions of the orientational states. These highly controlled cold collision experiments at the single partial wave limit allow the most direct comparison with the results of theoretical computations, necessary for accurate modeling of the molecular potential.

The recent development of the two-step SARP process, preparing higher vibrational states, has further widened the scope of probing long-range interactions. These weak interactions are substantially modified as the vibrationally excited molecule spends more time at the outer classical turning point of its anharmonic potential. A recent cold scattering experiment of SARP-prepared D_2 ($v = 4$) with Ne atom has already demonstrated the effect of vibrational excitation on long-range molecular forces. This study has showed that the $\Delta j = 2$ rotational relaxation of D_2 could not be observed unless the D_2 molecule is vibrationally excited to the $v = 4$ level.¹⁰⁹ It is expected that a highly vibrationally excited and rotationally aligned molecule will control the height of a reaction barrier. This combined with the possibility of resonance for low-temperature collision generates hope to experimentally study many exotic three-center and four-center exchange reactions with H_2 molecules. Although the four-center exchange reaction between a pair of H_2 molecules has been extensively studied theoretically, the dynamics of this benchmark reaction has remained controversial in the absence of a reliable experimental measurement. SARP's demonstrated ability to produce the rotationally aligned high vibrational states finally opens the possibility to experimentally study this four-center reaction, HD ($v = 4$) + HD ($v = 4$) $\rightarrow H_2 + D_2$.^{110–116}

Although aligned–aligned collisions have been demonstrated between a pair of SARP-prepared D_2 molecules, in these experiments SARP has controlled only a single molecular species. Experiment that independently controls the quantum states and alignments of both colliding partners can measure higher order vector correlations. To reach this goal, the experimental setup of the two-step SARP process that combines a delayed sequence of three laser pulses can be utilized to simultaneously prepare two different molecular species in desired quantum states. Finally, we note that SARP is not limited to only H_2 molecules; lightweight molecules such as HCl, H_2O , CH_4 , CO, N_2 , and C_2H_2 , whose rovibrational energy levels are separated by more than a few cm^{-1} , can also be prepared by SARP, giving the possibilities to experimentally study a wide variety of quantum-controlled scattering experiments.

■ AUTHOR INFORMATION

Corresponding Author

Nandini Mukherjee – Department of Chemistry, Stanford University, Stanford, California 94305, United States;
orcid.org/0000-0003-1486-8508; Email: nmukherj@stanford.edu

Complete contact information is available at:
<https://pubs.acs.org/10.1021/acs.jpca.2c06808>

Notes

The author declares no competing financial interest.

Biography



Nandini Mukherjee's goal is to understand how molecular collisions, which underly chemistry, take place at the most fundamental quantum level. Having done her Ph.D. work in coherent optical atomic physics, she gradually moved into the field of molecular physics, with a specific focus on the coherent control of chemical reactions. While working at the University of California at Los Angeles (UCLA) as Research Faculty, she studied molecular properties by developing a single-mode quantum cascade laser and proposed coherent control using infrared adiabatic passage processes. After joining Stanford University as a Senior Research Scientist, Nandini became interested in controlling the quantum states of hydrogen molecules, which was a standing challenge at that time. To meet this challenge, she proposed and developed the Stark-induced adiabatic Raman passage (SARP) method to control quantum states and orientations of hydrogen molecules and pioneered coherently controlled cold collisions in a molecular beam. To understand more about the quantum nature of chemical reactions, she plans to study fundamentally important reactive collisions by dressing reactants in a single or coherent superposition of quantum states.

ACKNOWLEDGMENTS

This work has been made possible by a grant from the National Science Foundation (Grant No. PHY- 2110256) and a grant from the U.S. Army Research Office through the MURI program (Grant W911NF-19-1-0283). The author thankfully acknowledges the continuous encouragement and support of Richard N. Zare in developing this field of research. The author acknowledges the sincere hard work of William Edward Perreault, who has contributed to this project first as a graduate student and later as a postdoctoral researcher. Sincere hard work and contribution of Haowen Zhou, the PhD graduate student working in this project, is also acknowledged. The author thanks Balakrishnan Naduvalath and Hua Guo for many helpful discussions.

REFERENCES

- (1) Gerber, R. B.; Buch, V.; Buck, U.; Maneke, G.; Schleusener, J. Direct Inversion of Rotationally Inelastic Cross Sections: Determination of the Anisotropic Ne-D₂ Potential. *Phys. Rev. Lett.* **1980**, *44* (21), 1397–1400.
- (2) Buck, U. Rotationally Inelastic Scattering of Hydrogen Molecules and the Non-Spherical Interaction. *Faraday Discuss. Chem. Soc.* **1982**, *73*, 187–203.
- (3) Herschbach, D. Molecular Collisions, from Warm to Ultracold. *Faraday Discuss.* **2009**, *142*, 9–23.
- (4) Krems, R. V. Cold Controlled Chemistry. *Phys. Chem. Chem. Phys.* **2008**, *10*, 4079–4092.
- (5) Weck, P. F.; Balakrishnan, N. Importance of Long-Range Interactions in Chemical Reactions at Cold and Ultracold Temperatures. *Int. Rev. Phys. Chem.* **2006**, *25* (3), 283–311.
- (6) Balakrishnan, N.; Dalgarno, A. Chemistry at Ultracold Temperatures. *Chem. Phys. Lett.* **2001**, *341* (5–6), 652–656.
- (7) Balakrishnan, N. On the Role of van Der Waals Interaction in Chemical Reactions at Low Temperatures. *J. Chem. Phys.* **2004**, *121* (12), 5563–5566.
- (8) Brumer, P.; Shapiro, M. Coherence Chemistry: Controlling Chemical Reactions with Lasers. *Acc. Chem. Res.* **1989**, *22* (12), 407–413.
- (9) Stuhl, B. K.; Hummon, M. T.; Ye, J. Cold State-Selected Molecular Collisions and Reactions. *Annu. Rev. Phys. Chem.* **2014**, *65*, 501–518.
- (10) Koch, C. P.; Shapiro, M. Coherent Control of Ultracold Molecules. *Chem. Rev.* **2012**, *112*, 4928–4948.
- (11) Chelkowski, S.; Bandrauk, A. D. Raman Chirped Adiabatic Passage: A New Method for Selective Excitation of High Vibrational States. *J. Raman Spectrosc.* **1997**, *28* (6), 459–466.
- (12) Yoder, B. L.; Bisson, R.; Morten Hundt, P.; Beck, R. D. Alignment Dependent Chemisorption of Vibrationally Excited CH₄(v₃) on Ni(100), Ni(110), and Ni(111). *J. Chem. Phys.* **2011**, *135* (22), 224703.
- (13) Loesch, H. J. Orientation and Alignment in Reactive Beam Collisions: Recent Progress. *Annu. Rev. Phys. Chem.* **1995**, *46*, 555–594.
- (14) Vitanov, N. V.; Fleischhauer, M.; Shore, B. W.; Bergmann, K. Coherent Manipulation of Atoms and Molecules by Sequential Laser Pulses. *Advances in Atomic, Molecular, and Optical Physics* **2001**, *46*, 55–190.
- (15) Alexander, A. J.; Brouard, M.; Kalogerakis, K. S.; Simons, J. P. *Chemistry with a Sense of Direction—the Stereodynamics of Bimolecular Reactions* **1998**, *27*, 405–415.
- (16) Perreault, W. E.; Mukherjee, N.; Zare, R. N. Quantum Control of Molecular Collisions at 1 K. *Science* **2017**, *358*, 356–359.
- (17) Perreault, W. E.; Mukherjee, N.; Zare, R. N. Quantum Controlled Rotationally Inelastic Scattering of HD with H₂ and D₂ near 1 K Reveals Collisional Partner Reorientation. *Nat. Chem.* **2018**, *10*, 561–567.
- (18) Zhou, H.; Perreault, W. E.; Mukherjee, N.; Zare, R. N. Shape Resonance Determined from Angular Distribution in D₂(v = 2, j = 2) + He → D₂(v = 2, j = 0) + He Cold Scattering. *J. Chem. Phys.* **2021**, *154* (10), 104309.
- (19) Perreault, W. E.; Mukherjee, N.; Zare, R. N. HD (v = 1, j = 2, m) Orientation Controls HD-He Rotationally Inelastic Scattering near 1 K. *J. Chem. Phys.* **2019**, *150* (17), 174301.
- (20) Zhou, H.; Perreault, W. E.; Mukherjee, N.; Zare, R. N. Quantum Mechanical Double Slit for Molecular Scattering. *Science* **2021**, *374*, 960–964.
- (21) Zhou, H.; Perreault, W. E.; Mukherjee, N.; Zare, R. N. Anisotropic Dynamics of Resonant Scattering between a Pair of Cold Aligned Diatoms. *Nat. Chem.* **2022**, *14* (6), 658–663.
- (22) Flower, D. *Molecular Collisions in the Interstellar Medium*, 2nd ed.; Cambridge University Press: 2007.
- (23) Sultanov, R. A.; Balakrishnan, N. Oxygen Chemistry in the Interstellar Medium: The Effect of Vibrational Excitation of H₂ in the O(³P)+H₂ Reaction. *Astrophys. J.* **2005**, *629* (1), 305–310.
- (24) Agundez, M.; Goicoechea, J.; Cernicharo, J.; Faure, A.; Roueff, E. The Chemistry of Vibrationally Excited H₂ in the Interstellar Medium. *Astrophys. J.* **2010**, *713*, 662.
- (25) Aoiz, F. J.; Brouard, M.; Gordon, S. D. S.; Nichols, B.; Stolte, S.; Walpole, V. A New Perspective: Imaging the Stereochemistry of Molecular Collisions. *Phys. Chem. Chem. Phys.* **2015**, *17* (45), 30210–30228.
- (26) Jones, E. M.; Brooks, P. R. Focusing and Orienting Asymmetric-Top Molecules in Molecular Beams. *J. Chem. Phys.* **1970**, *53* (1), 55–58.
- (27) Loesch, H. J.; Remscheid, A. Brute Force in Molecular Reaction Dynamics: A Novel Technique for Measuring Steric Effects. *J. Chem. Phys.* **1990**, *93* (7), 4779.

- (28) van Leuken, J. J.; van Amerom, F. H. W.; Bulthuis, J.; Snijders, J. G.; Stolte, S. Parity-Resolved Rotationally Inelastic Collisions of Hexapole State-Selected NO ($^2\Pi_{1/2}$, $J = 0.5$) with Ar. *J. Phys. Chem.* **1995**, *99*, 15573–15579.
- (29) Brouard, M.; Chadwick, H.; Gordon, S. D. S.; Hornung, B.; Nichols, B.; Klos, J.; Aoiz, F. J.; Stolte, S. Fully Quantum State-Resolved Inelastic Scattering of NO(X) + Kr: Differential Cross Sections and Product Rotational Alignment. *J. Chem. Phys.* **2014**, *141* (16), 164306.
- (30) Brouard, M.; Parker, D. H.; van de Meerakker, S. Y. T. Taming Molecular Collisions Using Electric and Magnetic Fields. *Chem. Soc. Rev.* **2014**, *43*, 7279–7294.
- (31) Rohlfing, E. A.; Chandler, D. W.; Parker, D. H. Direct Measurement of Rotational Energy Transfer Rate Constants for HCl ($v = 1$). *J. Chem. Phys.* **1987**, *87*, 5229–5237.
- (32) Dittmann, P.; Pesl, F. P.; Martin, J.; Coulston, G. W.; He, G. Z.; Bergmann, K. The Effect of Vibrational Excitation ($3 \leq v' \leq 19$) on the Reaction $\text{Na}_2(v') + \text{Cl} \rightarrow \text{NaCl} + \text{Na}^*$. *J. Chem. Phys.* **1992**, *97* (12), 9472.
- (33) Liu, K. Perspective: Vibrational-Induced Steric Effects in Bimolecular Reactions. *J. Chem. Phys.* **2015**, *142* (8), 080901.
- (34) Vitanov, N. V.; Halfmann, T.; Shore, B. W.; Bergmann, K. Laser-Induced Population Transfer By Adiabatic Passage Techniques. *Annu. Rev. Phys. Chem.* **2001**, *52*, 763–809.
- (35) Mukherjee, N.; Zare, R. N. Preparation of Polarized Molecules Using Coherent Infrared Multicolor Ladder Excitation. *J. Chem. Phys.* **2010**, *132* (15), 154302.
- (36) Mukherjee, N.; Perreault, W. E.; Zare, R. N. *Stark-Induced Adiabatic Passage Processes to Selectively Prepare Vibrationally Excited Single and Superposition of Quantum States*; Laane, J., Ed.; Elsevier Inc.: 2017. DOI: 10.1016/B978-0-12-811220-5.00001-0.
- (37) Mukherjee, N.; Zare, R. N. Can Stimulated Raman Pumping Cause Large Population Transfers in Isolated Molecules? *J. Chem. Phys.* **2011**, *135* (18), 184202.
- (38) Mukherjee, N.; Zare, R. N. Stark-Induced Adiabatic Raman Passage for Preparing Polarized Molecules. *J. Chem. Phys.* **2011**, *135* (2), 024201.
- (39) Mukherjee, N.; Dong, W.; Harrison, J. A.; Zare, R. N. Communication: Transfer of More than Half the Population to a Selected Rovibrational State of H_2 by Stark-Induced Adiabatic Raman Passage. *J. Chem. Phys.* **2013**, *138* (5), 051101.
- (40) Dong, W.; Mukherjee, N.; Zare, R. N. Optical Preparation of H_2 Rovibrational Levels with Almost Complete Population Transfer. *J. Chem. Phys.* **2013**, *139* (7), 074204.
- (41) Mukherjee, N.; Perreault, W. E.; Zare, R. N. Stark-Induced Adiabatic Raman Ladder for Preparing Highly Vibrationally Excited Quantum States of Molecular Hydrogen. *J. Phys. B At. Mol. Opt. Phys.* **2017**, *50* (14), 144005.
- (42) Perreault, W. E.; Mukherjee, N.; Zare, R. N. Preparation of a Selected High Vibrational Energy Level of Isolated Molecules. *J. Chem. Phys.* **2016**, *145* (15), 154203.
- (43) Mukherjee, N.; Perreault, W. E.; Zare, R. N. Stark-Induced Adiabatic Passage Processes to Selectively Prepare Vibrationally Excited Single and Superposition of Quantum States. In *Frontiers and Advances in Molecular Spectroscopy*; Elsevier Inc.: Cambridge, MA, 2018; pp 1–46.
- (44) Perreault, W. E.; Zhou, H.; Mukherjee, N.; Zare, R. N. Harnessing the Power of Adiabatic Curve Crossing to Populate the Highly Vibrationally Excited H_2 ($v = 7, j = 0$) Level. *Phys. Rev. Lett.* **2020**, *124*, 163202.
- (45) Perreault, W. E.; Mukherjee, N.; Zare, R. N. Stark-Induced Adiabatic Raman Passage Examined through the Preparation of D_2 ($v = 2, j = 0$) and D_2 ($v = 2, j = 2, m = 0$). *J. Chem. Phys.* **2019**, *150* (23), 234201.
- (46) Mukherjee, N.; Dong, W.; Zare, R. N. Coherent Superposition of M-States in a Single Rovibrational Level of H_2 by Stark-Induced Adiabatic Raman Passage. *J. Chem. Phys.* **2014**, *140* (7), 074201.
- (47) Seideman, T. Revival Structure of Aligned Rotational Wave Packets. *Phys. Rev. Lett.* **1999**, *83* (24), 4971–4974.
- (48) Rosca-Pruna, F.; Vrakking, M. J. J. Experimental Observation of Revival Structures in Picosecond Laser-Induced Alignment of I₂. *Phys. Rev. Lett.* **2001**, *87* (15), 153902.
- (49) Renard, M.; Hertz, E.; Gurin, S.; Jauslin, H. R.; Lavorel, B.; Faucher, O. Control of Field-Free Molecular Alignment by Phase-Shaped Laser Pulses. *Phys. Rev. A - At. Mol. Opt. Phys.* **2005**, *72* (2), 1–4.
- (50) Son, H.; Park, J. J.; Lu, Y.; Jamison, A. O.; Karman, T.; Ketterle, W. Control of Reactive Collisions by Quantum Interference. *Science* **2022**, *375*, 1006–1010.
- (51) Paliwal, P.; Deb, N.; Reich, D. M.; van der Avoird, A.; Koch, C. P.; Narevicius, E. Determining the Nature of Quantum Resonances by Probing Elastic and Reactive Scattering in Cold Collisions. *Nat. Chem.* **2021**, *13* (1), 94–98.
- (52) Naulin, C.; Costes, M. Experimental Search for Scattering Resonances in near Cold Molecular Collisions. *Int. Rev. Phys. Chem.* **2014**, *33* (4), 427–446.
- (53) Costes, M.; Naulin, C. Observation of Quantum Dynamical Resonances in near Cold Inelastic Collisions of Astrophysical Molecules. *Chem. Sci.* **2016**, *7* (4), 2462–2469.
- (54) Quémener, G.; Julienne, P. S. Ultracold Molecules under Control! *Chem. Rev.* **2012**, *112* (9), 4949–5011.
- (55) Köhler, T.; Góral, K.; Julienne, P. S. Production of Cold Molecules via Magnetically Tunable Feshbach Resonances. *Rev. Mod. Phys.* **2006**, *78* (4), 1311–1361.
- (56) Onvlee, J.; van der Avoird, A.; Groenenboom, G.; Van De Meerakker, S. Y. T. Probing Scattering Resonances in (Ultra)Cold Inelastic NO-He Collisions. *J. Phys. Chem. A* **2016**, *120* (27), 4770–4777.
- (57) Chefdeville, S.; Kalugina, Y.; van de Meerakker, S. Y. T.; Naulin, C.; Lique, F.; Costes, M. Observation of Partial Wave Resonances in Low-Energy $\text{O}_2\text{-H}_2$ Inelastic Collisions. *Science* **2013**, *341* (6150), 1094–1096.
- (58) Croft, J. F. E.; Balakrishnan, N.; Huang, M.; Guo, H. Unraveling the Stereodynamics of Cold Controlled HD- H_2 Collisions. *Phys. Rev. Lett.* **2018**, *121* (11), 113401.
- (59) Lee, T.-G.; Balakrishnan, N.; Forrey, R. C.; Stancil, P. C.; Schultz, D. R.; Ferland, G. J. State-to-State Rotational Transitions in $\text{H}_2 + \text{H}_2$ Collisions at Low Temperatures. *J. Chem. Phys.* **2006**, *125*, 114302.
- (60) Ospelkaus, S.; Ni, K. K.; Wang, D.; de Miranda, M. H. G.; Neyenhuis, B.; Quémener, G.; Julienne, P. S.; Bohn, J. L.; Jin, D. S.; Ye, J. Quantum-State Controlled Chemical Reactions of Ultracold Potassium-Rubidium Molecules. *Science* **2010**, *327* (2010), 853–857.
- (61) Hu, M. G.; Liu, Y.; Grimes, D. D.; Lin, Y. W.; Gheorghe, A. H.; Vexiau, R.; Bouloufa-Maafa, N.; Dulieu, O.; Rosenband, T.; Ni, K. K. Direct Observation of Bimolecular Reactions of Ultracold KRb Molecules. *Science* **2019**, *366* (6469), 1111–1115.
- (62) Ni, K. K.; Ospelkaus, S.; Wang, D.; Quémener, G.; Neyenhuis, B.; De Miranda, M. H. G.; Bohn, J. L.; Ye, J.; Jin, D. S. Dipolar Collisions of Polar Molecules in the Quantum Regime. *Nature* **2010**, *464* (7293), 1324–1328.
- (63) van de Meerakker, S. Y.; Bethlem, H. L.; Vanhaecke, N.; Meijer, G. Manipulation and Control of Molecular Beams. *Chem. Rev.* **2012**, *112* (9), 4828–4878.
- (64) Amarasinghe, C.; Suits, A. G. Intrabeam Scattering for Ultracold Collisions. *J. Phys. Chem. Lett.* **2017**, *8*, 5153–5159.
- (65) Amarasinghe, C.; Perera, C. A.; Suits, A. G. A Versatile Molecular Beam Apparatus for Cold/Ultracold Collisions. *J. Chem. Phys.* **2020**, *152* (18), 184201.
- (66) Naulin, C.; Costes, M. Experimental Search for Scattering Resonances in near Cold Molecular Collisions. *Int. Rev. Phys. Chem.* **2014**, *33* (4), 427–446.
- (67) Chefdeville, S.; Stoecklin, T.; Bergeat, A.; Hickson, K. M.; Naulin, C.; Costes, M. Appearance of Low Energy Resonances in CO-Para- H_2 Inelastic Collisions. *Phys. Rev. Lett.* **2012**, *109* (2), 023201.
- (68) de Jongh, T.; Besemer, M.; Shuai, Q.; Karman, T.; van der Avoird, A.; Groenenboom, G. C.; van de Meerakker, S. Y. T. Imaging the Onset of the Resonance Regime in Low-Energy NO-He Collisions. *Science* **2020**, *368* (May), 626–630.

- (69) Vogels, S. N.; Karman, T.; Klos, J.; Besemer, M.; Onvlee, J.; van der Avoird, A.; Groenenboom, G. C.; van de Meerakker, S. Y. T. Scattering Resonances in Bimolecular Collisions between NO Radicals and H₂ Challenge the Theoretical Gold Standard. *Nat. Chem.* **2018**, *10*, 435–440.
- (70) Shagam, Y.; Narevicius, E. Sub-Kelvin Collision Temperatures in Merged Neutral Beams by Correlation in Phase-Space. *J. Phys. Chem. C* **2013**, *117* (43), 22454–22461.
- (71) Klein, A.; Shagam, Y.; Skomorowski, W.; Zuchowski, P. S.; Pawlak, M.; Janssen, L. M. C.; Moiseyev, N.; Van De Meerakker, S. Y. T.; Van Der Avoird, A.; Koch, C. P.; Narevicius, E. Directly Probing Anisotropy in Atom-Molecule Collisions through Quantum Scattering Resonances. *Nat. Phys.* **2017**, *13* (1), 35–38.
- (72) Jankunas, J.; Osterwalder, A. Cold and Controlled Molecular Beams: Production and Applications. *Annu. Rev. Phys. Chem.* **2015**, *66* (1), 241–262.
- (73) Bertsche, B.; Jankunas, J.; Osterwalder, A. Low-Temperature Collisions between Neutral Molecules in Merged Molecular Beams. *Chimia* **2014**, *68* (4), 256–259.
- (74) Osterwalder, A. Merged Neutral Beams. *EPJ. Technol. Instrum.* **2015**, *2* (1), 1–28.
- (75) Shagam, Y.; Klein, A.; Skomorowski, W.; Yun, R.; Averbukh, V.; Koch, C. P.; Narevicius, E. Molecular Hydrogen Interacts More Strongly When Rotationally Excited at Low Temperatures Leading to Faster Reactions. *Nat. Chem.* **2015**, *7* (11), 921–926.
- (76) Yang, B.; Zhang, P.; Wang, X.; Stancil, P. C.; Bowman, J. M.; Balakrishnan, N.; Forrey, R. C. Quantum Dynamics of CO-H₂ in Full Dimensionality. *Nat. Commun.* **2015**, *6*, 1–8.
- (77) Balakrishnan, N.; Quémener, G.; Forrey, R. C.; Hinde, R. J.; Stancil, P. C. Full-Dimensional Quantum Dynamics Calculations of H₂-H₂ Collisions. *J. Chem. Phys.* **2011**, *134* (1), 014301.
- (78) Balakrishnan, N.; Forrey, R.; Dalgarno, A. Threshold Phenomena in Ultracold Atom-Molecule Collisions. *Chem. Phys. Lett.* **1997**, *280* (1–2), 1–4.
- (79) Bergeat, A.; Onvlee, J.; Naulin, C.; Van Der Avoird, A.; Costes, M. Quantum Dynamical Resonances in Low-Energy CO(*j* = 0) + He Inelastic Collisions. *Nat. Chem.* **2015**, *7* (4), 349–353.
- (80) Zhou, H.; Perreault, W. E.; Mukherjee, N.; Zare, R. N. Shape Resonance Determined from Angular Distribution in D₂ (*v* = 2, *j* = 2) + He → D₂ (*v* = 2, *j* = 0) + He Cold Scattering. *J. Chem. Phys.* **2021**, *154* (10), 104309.
- (81) Forrey, R.; Balakrishnan, N.; Dalgarno, A.; Haggerty, M.; Heller, E. Quasiresonant Energy Transfer in Ultracold Atom-Diatom Collisions. *Phys. Rev. Lett.* **1999**, *82* (13), 2657–2660.
- (82) Balakrishnan, N.; Forrey, R. C.; Dalgarno, A. Quenching of H₂ Vibrations in Ultracold ³He and ⁴He Collisions. *Phys. Rev. Lett.* **1998**, *80* (15), 3224–3227.
- (83) Kendrick, B. K.; Hazra, J.; Balakrishnan, N. Geometric Phase Effects in the Ultracold H+H₂ Reaction. *J. Chem. Phys.* **2016**, *145* (16), 164303.
- (84) Simbotin, I.; Ghosal, S.; Côté, R. A Case Study in Ultracold Reactive Scattering: D + H₂. *Phys. Chem. Chem. Phys.* **2011**, *13* (42), 19148–19155.
- (85) Uudus, N.; Magaki, S.; Balakrishnan, N. Quantum Mechanical Investigation of Rovibrational Relaxation of H₂ and D₂ by Collisions with Ar Atoms. *J. Chem. Phys.* **2005**, *122* (2), 024304.
- (86) Reuss, J.; Stolte, S. Calculation of the Total Collision Cross Section of H₂ for a Particular Rotation *j*, *m_j*-State of the H₂ Molecule. *Physica* **1969**, *42*, 111–123.
- (87) Quémener, G.; Balakrishnan, N.; Krems, R. V. Vibrational Energy Transfer in Ultracold Molecule-Molecule Collisions. *Phys. Rev. A - At. Mol. Opt. Phys.* **2008**, *77* (3), 1–4.
- (88) Arnold, J.; Dreier, T.; Chandler, D. W. Rotational and Vibrational Energy Transfer of H₂ (*v* = 1, *J* = 1) in Collisions with H₂, Ar, HD and D₂. *Chem. Phys.* **1989**, *133*, 123–136.
- (89) Buck, U. Rotationally Inelastic Scattering of Hydrogen Molecules and the Non-Spherical Interaction. *Faraday Discuss. Chem. Soc.* **1982**, *73*, 187–203.
- (90) Rohlfling, E. A.; Rabitz, H.; Gelfand, J.; Miles, R. B. Mechanisms and Rate Constants for the Vibrational Relaxation of HD (*v* = 4, 5, and 6) in Collisions with HD, ⁴He, and D₂. *J. Chem. Phys.* **1984**, *81* (2), 820–827.
- (91) Buck, U.; Huiskens, F.; Kohlhase, A.; Otten, D.; Schaefer, J. State Resolved Rotational Excitation in D₂+H₂ Collisions. *J. Chem. Phys.* **1983**, *78* (1983), 4439–4450.
- (92) Chandler, D. W.; Farrow, R. L. Measurement of Rotational Energy-Transfer Rates for HD (*v* = 1) in Collisions with Thermal HD. *J. Chem. Phys.* **1986**, *85* (2), 810–816.
- (93) Perreault, W. E.; Mukherjee, N.; Zare, R. N. Supersonic Beams of Mixed Gases: A Method for Studying Cold Collisions. *Chem. Phys.* **2018**, *514*, 150–153.
- (94) Perreault, W. E.; Mukherjee, N.; Zare, R. N. Angular and Internal State Distributions of H₂⁺ Generated by (2 + 1) Resonance Enhanced Multiphoton Ionization of H₂ Using Time-of-Flight Mass Spectrometry. *J. Chem. Phys.* **2016**, *144* (21), 214201.
- (95) Shore, B. W. The Schrodinger Atom. In *The Theory of Coherent Atomic Excitation*; John Wiley & Sons: New York, 1990; pp 187–262.
- (96) Perreault, W. E.; Zhou, H.; Mukherjee, N.; Zare, R. N. Coherent Preparation of Highly Vibrating and Rotating D₂ Molecules. *J. Phys. Chem. Lett.* **2022**, *13* (21), 4682–4687.
- (97) Croft, J. F. E.; Balakrishnan, N. Controlling Rotational Quenching Rates in Cold Molecular Collisions. *J. Chem. Phys.* **2019**, *150* (16), 164302.
- (98) Brouard, M.; Burak, I.; Hughes, D. W.; Kalogerakis, K. S.; Simons, J. P.; Stavros, V. c. Product State Resolved Stereodynamics: Rotational Polarization of OH(²Π;*v*’,*N*’,Ω,*f*) Scattered from the Reaction, H+CO₂→OH+CO. *J. Chem. Phys.* **2000**, *113* (8), 3173–3180.
- (99) Nichols, B.; Chadwick, H.; Gordon, S. D. S.; Eyles, C. J.; Hornung, B.; Brouard, M.; Alexander, M. H.; Aoiz, F. J.; Gijbtsen, A.; Stolte, S. Steric Effects and Quantum Interference in the Inelastic Scattering of NO(*X*) + Ar. *Chem. Sci.* **2015**, *6* (4), 2202–2210.
- (100) Jambrina, P. G.; Croft, J. F. E.; Guo, H.; Brouard, M.; Balakrishnan, N.; Aoiz, F. J. Stereodynamical Control of a Quantum Scattering Resonance in Cold Molecular Collisions. *Phys. Rev. Lett.* **2019**, *123* (4), 43401.
- (101) Onvlee, J.; Gordon, S. D. S.; Vogels, S. N.; Auth, T.; Karman, T.; Nichols, B.; van der Avoird, A.; Groenenboom, G. C.; Brouard, M.; van de Meerakker, S. Y. T. Imaging Quantum Stereodynamics through Fraunhofer Scattering of NO Radicals with Rare-Gas Atoms. *Nat. Chem.* **2017**, *9* (3), 226–233.
- (102) Perreault, W. E.; Zhou, H.; Mukherjee, N.; Zare, R. N. A Bi-Axial Quantum State That Controls Molecular Collisions Like a Double-Slit Interferometer. *Front. Phys.* **2021**, *9* (May), 671997.
- (103) Andres, J.; Buck, U.; Huiskens, F.; Schleusener, J.; Torello, F. The Anisotropic Interaction Potential of D₂Ne from State-to-State Differential Cross Sections for Rotational Excitation. *J. Chem. Phys.* **1980**, *73*, 5620–5630.
- (104) Buck, U.; Huiskens, F.; Schleusener, J.; Schaefer, J. State Resolved Rotational Excitation in HD+D₂ Collisions. I. Angular Dependence of 0→2 Transitions. *J. Chem. Phys.* **1981**, *74*, 535–544.
- (105) Blatt, J. M.; Biedenharn, L. C. The Angular Distribution of Scattering and Reaction Cross Sections. *Rev. Mod. Phys.* **1952**, *24* (4), 258–272.
- (106) Arthurs, A. M.; Dalgarno, A. The Theory of Scattering by a Rigid Rotator. *Proc. R. Soc. A* **1960**, *256* (1287), 540–551.
- (107) Jambrina, P. G.; Morita, M.; Croft, J. F. E.; Aoiz, F. J.; Balakrishnan, N. Role of Low Energy Resonances in the Stereodynamics of Cold He + D₂ Collisions. *J. Phys. Chem. Lett.* **2022**, *13*, 4064–4072.
- (108) Morita, M.; Balakrishnan, N. Stereodynamics of Rotationally Inelastic Scattering in Cold He + HD Collisions. *J. Chem. Phys.* **2020**, *153* (9), 091101.
- (109) Perreault, W. E.; Zhou, H.; Mukherjee, N.; Zare, R. N. Resonant Cold Scattering of Highly Rotationally Excited D₂ with Ne. *J. Chem. Phys.* **2022**, *157*, 144301.

- (110) Brown, N. J.; Silver, D. M. Reactive and Inelastic Scattering of H_2+D_2 Using a Repulsive Model Potential Energy Surface. *J. Chem. Phys.* **1978**, *68* (8), 3607–3617.
- (111) Silver, D. M. Reaction Paths for Bimolecular Hydrogen Exchange. *Chem. Phys. Lett.* **1972**, *14*, 105–107.
- (112) Bauer, S. H.; Ossa, E. Isotope Exchange Rates. III. The Homogeneous Four-Center Reaction H_2+D_2 . *J. Chem. Phys.* **1966**, *45* (2), 434–443.
- (113) Hernández, M. I.; Clary, D. C. Four-Center Reactions: A Quantal Model for H_4 . *J. Chem. Phys.* **1996**, *104* (21), 8413–8423.
- (114) Bauer, S. H. Four Center Metathesis Reactions. *Annu. Rev. Phys. Chem.* **1979**, *30* (1), 271–310.
- (115) Burcat, A.; Lifshitz, A. Further Studies on the Homogeneous Exchange Reaction H_2+D_2 . *J. Chem. Phys.* **1967**, *47* (8), 3079.
- (116) Bauer, S. H.; Lederman, D. M.; Resler, E. L.; Fisher, E. R. The Homogeneous Gas Phase $\text{H}_2\text{-D}_2$ Metathesis at Room Temperature: Reaction Induced by Specific Vibrational Excitation. *Int. J. Chem. Kinet.* **1973**, *5* (1), 93–106.
- (117) Bakr, B. W.; Smith, D. G. A.; Patkowski, K. Highly Accurate Potential Energy Surface for the He- H_2 Dimer. *J. Chem. Phys.* **2013**, *139* (14), 144305.